

HiResCAM: Faithful Location Representation in Visual Attention for Explainable 3D Medical Image Classification

Rachel Léa Draelos
Computer Science Department
Duke University
rlb61@duke.edu

Lawrence Carin
ECE Department
Duke University
lcarin@duke.edu

Abstract

Understanding model predictions is critical in healthcare, to facilitate rapid verification of model correctness and to guard against the use of models that exploit confounding variables. Here we address the challenging new task of explainable multilabel classification of volumetric medical images. We first illustrate a previously unrecognized limitation of the popular model explanation method Grad-CAM: as a side effect of the gradient averaging step, Grad-CAM sometimes highlights the wrong location. To solve this problem, we propose HiResCAM, a novel label-specific attention mechanism that is guaranteed to highlight only the locations the model used to make each prediction. Next, we introduce a mask loss that leverages HiResCAM to encourage the model to predict abnormalities based only on the organs in which those abnormalities appear. Our innovations result in a 37% improvement in explanation quality, resulting in state-of-the-art weakly supervised organ localization of multiple abnormalities in the RAD-ChestCT data set of 36,316 CT volumes. We also demonstrate on PASCAL VOC 2012 the different properties of HiResCAM and Grad-CAM on natural images. Overall, this work advances convolutional neural network explanation approaches and the clinical applicability of multiple abnormality modeling in volumetric medical images.

1. Introduction

Automated interpretation of medical images with machine learning has the potential to revolutionize the field of radiology. However, machine learning systems have not yet been adopted on a large scale in clinical practice [3]. One barrier to adoption is trust [47, 54]. Most medical imaging models are based on convolutional neural networks, which are “black box” models unless additional steps are taken to improve explainability [4].

An explainable model in computer vision indicates

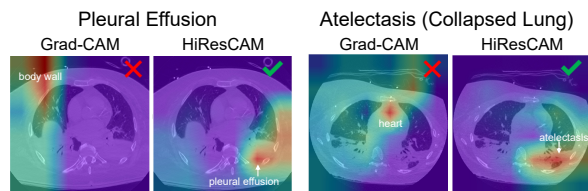


Figure 1. Examples of Grad-CAM creating the incorrect impression that the model focused on the wrong anatomical structure. The HiResCAM and Grad-CAM explanations were generated using exactly the same model on the same input volume. The only difference is the explanation method. Both of these abnormalities are lung findings. However, Grad-CAM creates the impression that the model predicted these abnormalities based on the body wall and heart, which are irrelevant. HiResCAM faithfully reveals the true locations that the model used, which were in the lungs after all. Best viewed in color. Text annotations added for clarity.

which regions of the image contribute to its predictions [4]. Explainability is critical in medical imaging to detect situations where a model leverages aspects of the data that are correlated with an outcome but inappropriate for prediction. Zech *et al.* [77] used class activation mapping [79] to reveal that a CNN trained to predict pneumonia from chest radiographs leveraged non-medical features to make the pneumonia prediction. Specifically, the CNN identified differences in metal tokens, postprocessing, and compression artefacts which identified the hospital system of origin, a highly effective indicator of pneumonia risk due to differing frequencies of pneumonia among the patient populations. Furthermore, a “model” consisting of sorting the radiographs by hospital system achieved an AUROC of 0.861, illustrating that high performance alone does not guarantee that a model is faithful to expected medical reasoning. This behavior is analogous to natural image classifiers detecting boats via water, trains via rails, or horses via a copyright watermark [40, 41]. It is thus critical to seek insight into how models make their predictions.

In this work, we consider explainable multilabel classi-

fication in volumetric medical images. Our contributions include:

- High-Resolution Class Activation Mapping (HiResCAM), a new region-focused attention mechanism that identifies the locations in the input volume that most contribute to prediction of each abnormality;
- PARTITION, an approach to obtain pixel-level allowed regions for each abnormality without any manual labeling by combining unsupervised multi-organ segmentation with location information from radiology reports;
- A mask loss that leverages HiResCAM and the PARTITION allowed regions to encourage the model to predict abnormalities from within the organs in which they are found.

Our combined innovations yield state-of-the-art performance on explainable multi-abnormality prediction in 3D medical images.

2. Related Work

Abnormality prediction in chest CT scans. CT scans are used to diagnose and monitor numerous conditions, including cancer [60], injuries [50], and lung disease [15, 53]. CT scans and natural images differ significantly. Natural images are typically 2D RGB images in which each pixel belongs to only one class and the colors, shapes, and textures of each class are distinct enough for the average human to appreciate the difference (*e.g.* “cat” vs. “dog”). In contrast, CT scans are grayscale volumetric images on the order of 70,000,000 pixels each ($\approx 500\times$ larger than natural images), in which each pixel could belong to multiple classes due to physically overlapping diseases. Furthermore, the color, shape, and texture of each class can be challenging to distinguish even for domain experts, due to heterogeneity within one disease and similarities across different diseases [20, 21, 25, 18].

Due to the challenging and time-consuming nature of CT interpretation, there has been substantial interest in developing machine learning models to analyze CT scans. Almost all prior work in CT classification has focused on one abnormality at a time, such as interstitial lung disease [10, 68, 27, 26, 67, 13, 5], lung cancer [6], pneumothorax [46], or emphysema [33].

The only model developed to predict multiple abnormalities simultaneously from one CT volume is CT-Net [20], which was trained and evaluated on the RAD-ChestCT data set of 36,316 CT volumes annotated with 83 whole-volume abnormality labels each. While CT-Net achieves high performance, its final representation is not interpretable due to an intermediate convolution step over the feature dimension

that disrupts the spatial relationship between the representation and the input volume. Our proposed model outperforms CT-Net while providing explainability.

Gradient-based neural network explanation methods. Our proposed attention mechanism, HiResCAM, is part of the family of gradient-based neural network explanation methods [4].

Input-level approaches. Saliency mapping [62], DeconvNets [78], and Guided Backpropagation [63] are gradient-based explanation methods that compute the gradient of the class score with respect to the input image, to visualize important image regions. These methods are identical except for handling of ReLU nonlinearities [49]. Gradient * Input [61] is a related method in which the gradient of the class score with respect to the input is multiplied element-wise against the input itself. Layer-wise relevance propagation (LRP) [7] proceeds layer-by-layer, starting with the output, to redistribute the final score across the pixels of the input layer. While not originally formulated as a gradient-based explanation method, ϵ -LRP is in fact equivalent to Gradient * Input where the gradient is calculated in a modified manner using the ratio between the output and input at each nonlinearity [4]. A limitation of the aforementioned approaches is the “white noise” appearance of the final explanation caused by noisy gradients [8, 49].

Output-level approaches. Class Activation Mapping (CAM) [79] is an explanation method for a particular class of models that consist of convolutions followed by global average pooling over features and one final fully connected layer. The explanations are produced by multiplying the class-specific weights of the final layer by the corresponding feature maps prior to pooling. CAM may be considered a gradient-based method, as the final class-specific weights are the gradient of the score with respect to the feature maps. Grad-CAM [58] is a generalization of CAM, in which gradients are averaged over the spatial dimensions to produce importance weights. The Grad-CAM explanation is a sum of feature maps weighted by the importance weights.

Unlike the input-level approaches, which rely on propagation through all layers back to the level of the original image, CAM and Grad-CAM produce explanations at a layer of the network closer to the output. The low-dimensional explanation is then upsampled for superimposition over the input image, an acceptable step because typical CNNs preserve spatial relationships. Guided Grad-CAM [58] is a Grad-CAM variant obtained via an element-wise product of the Guided Backpropagation [63] and Grad-CAM explanations.

Recent work has called into question some gradient-based explanation methods. Nie *et al.* [49] demonstrate that Guided Backpropagation and DeconvNets perform partial image recovery due to their handling of ReLU nonlineari-

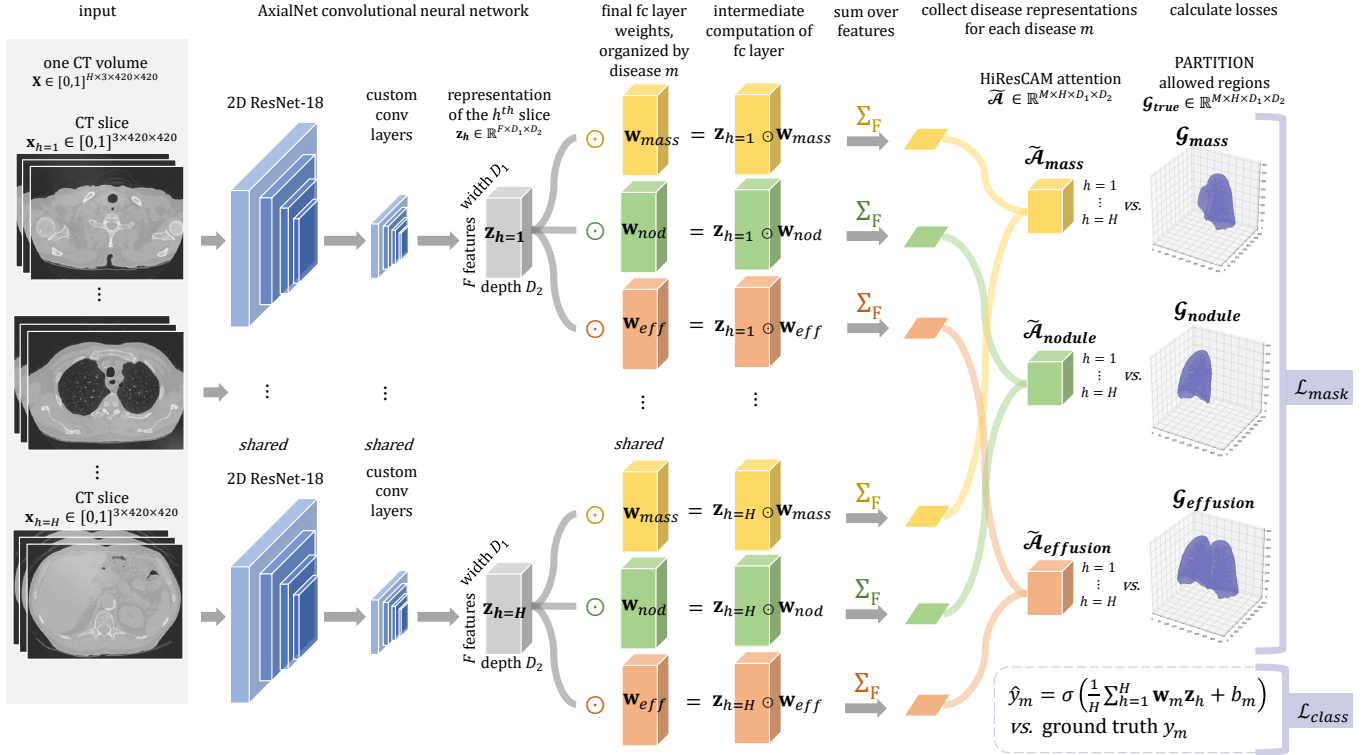


Figure 2. Calculation of the proposed HiResCAM abnormality-specific attention and losses for AxialNet. A low-dimensional representation \mathbf{z}_h is obtained for each slice $h = 1, \dots, H$ via 2D convolutions on axial slices. A final fully connected layer produces M abnormality scores per slice. The slice scores are averaged for each abnormality to produce the overall score used in the classification loss (lower right). A HiResCAM attention map is calculated for each abnormality as the element-wise product of the representation \mathbf{z}_h with the gradient of the abnormality score with respect to \mathbf{z}_h , summed over the feature dimension. In AxialNet, this gradient is equal to the fully connected layer weights for the relevant abnormality (Section 3.4). The mask loss (Section 3.5) is computed using the HiResCAM attention maps and allowed regions \mathcal{G}_{true} to encourage the model to only increase the abnormality score using organs in which that abnormality is found. Here, the allowed organs are the left lung for mass, the right lung for nodule, and both lungs for pleural effusion.

ties and max pooling. Adebayo *et al.* [1] reveal that Guided Backpropagation, Guided Grad-CAM, and Gradient * Input produce convincing explanations even when model parameters have been randomized or when a model has been trained on randomly labeled data. However, saliency mapping and Grad-CAM pass the sanity checks.

Because they are class-specific and produce less noisy explanations than input-level methods, CAM and Grad-CAM form the foundation of numerous methods for weakly supervised localization [38, 71, 69, 32, 72, 35, 70, 23, 2, 24, 11, 12, 44, 43], and have also been widely used in medical imaging applications [42, 51, 9, 59, 52, 48].

We propose a new explanation method, HiResCAM, with connections to Grad-CAM and Gradient * Input that are explored further in Section 3.4. We demonstrate that HiResCAM outperforms Grad-CAM, producing quantitatively and qualitatively improved explanations for volumetric medical images.

3. Methods

3.1. Problem setup

Consider a dataset $\{\mathbf{X}, \mathbf{y}\}_{i=1}^N$ where $\mathbf{y}_i \in \{0, 1\}^M$ is a binary vector corresponding to the presence/absence of M abnormalities and $\mathbf{X}_i \in [0, 1]^{405 \times 420 \times 420}$ is a CT volume.¹ We wish to predict, in an explainable manner, the labels $\hat{\mathbf{y}}_i$ given a CT volume \mathbf{X}_i , meaning that for any abnormality $m \in \{1, 2, \dots, M\}$ a physician can query the model to retrieve the sub-region within the volume that is most predictive of that abnormality. Figure 2 provides an overview of our solution to this task.

3.2. Modeling

Radiologists typically view CT scans as a stack of axial slices [73], which form horizontal planes through an upright patient. Motivated by this practice, we propose Axial-

¹ $\mathbf{X}_i \in [0, 1]^{135 \times 3 \times 420 \times 420}$ is used when three adjacent slices are grouped to enable use of a feature extractor pre-trained on ImageNet.

Net, a multiple instance learning architecture that facilitates determination of which axial slices contribute the most to prediction of each abnormality, and enables the most interpretable use of HiResCAM. First, a 2D CNN is applied to each CT slice. The CNN’s parameters are shared across slices (Figure 2), an approach that has been previously successful in CT analysis [20, 45, 57]. The low-dimensional representation produced by the CNN for the h^{th} slice is termed $\mathbf{z}_h \in \mathbb{R}^{F \times D_1 \times D_2}$ with F features, width D_1 , and depth D_2 . It will be used in the proposed attention mechanism HiResCAM as well as the proposed mask loss. An abnormality score vector $\mathbf{c}_h \in \mathbb{R}^M$ is produced for each slice representation \mathbf{z}_h using a fully-connected layer with parameters shared across all CT slices: $\mathbf{c}_h = \mathbf{W}\mathbf{z}_h + \mathbf{b}$, with $\mathbf{W} \in \mathbb{R}^{M \times F D_1 D_2}$ and $\mathbf{b} \in \mathbb{R}^M$. The matrix of all per-slice abnormality scores $\mathbf{C} \in \mathbb{R}^{M \times H}$ provides model explainability by illustrating which axial slices contribute most to the prediction of each abnormality. The final whole-volume abnormality score s_m is produced for each abnormality by averaging the per-slice abnormality scores:

$$s_m = \frac{1}{H} \sum_{h=1}^H \mathbf{w}_m \mathbf{z}_h + b_m, \quad (1)$$

where one row vector $\mathbf{w}_m \in \mathbb{R}^{F D_1 D_2}$ of the weight matrix \mathbf{W} corresponds to one abnormality, meaning that the expression $\mathbf{w}_m \mathbf{z}_h + b_m$ produces the scalar score c_{mh} for the m^{th} abnormality and h^{th} slice.

Finally, the whole-volume predicted probability \hat{y}_m for the m^{th} abnormality is calculated from the whole-volume score s_m using the sigmoid function $\hat{y}_m = \sigma(s_m) = \frac{1}{1+e^{-s_m}}$. For each observation we optimize the expected multilabel cross entropy objective, requiring only whole-volume abnormality labels:

$$\mathcal{L}_{class} = -\frac{1}{M} \sum_{m=1}^M [y_m \log \hat{y}_m + (1 - y_m) \log(1 - \hat{y}_m)]. \quad (2)$$

3.3. Proposed HiResCAM for abnormality-specific attention

We propose an attention mechanism, High-Resolution Class Activation Mapping (HiResCAM), which produces for every abnormality $m = 1, \dots, M$ an abnormality-specific attention map $\hat{\mathbf{A}}_m^{\text{HiResCAM}} \in \mathbb{R}^{H \times D_1 \times D_2}$, *i.e.* attention over the spatial dimensions (excluding the feature dimension F). The abnormality-specific attention maps provide sub-slice localization to further improve explainability and to enable calculation of the mask loss (Section 3.5).

HiResCAM is inspired by the popular attention mechanism Grad-CAM [58], and is designed to address a limitation of the Grad-CAM averaging step. In Grad-CAM,

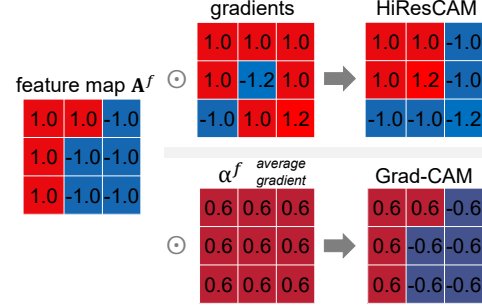


Figure 3. 2D example of how HiResCAM addresses the limitation of the gradient averaging step in Grad-CAM. The Grad-CAM attention map (equation(4)) matches the relative magnitudes and positive-negative pattern of the original feature map (the “inverted red L shape” in this example), even though the gradients suggest that some elements should be re-scaled and/or change sign. HiResCAM (equation (17)) does not average over the gradients and instead element-wise multiplies the feature map with the gradients directly, thereby producing attention that more accurately reflects the model’s computations and emphasizes the most important *locations* for a particular prediction. Best viewed in color.

feature map importance weights α^f are calculated by averaging gradients over the spatial dimensions of the low-dimensional CT representation. Such averaging is likely inspired by the global average pooling step built in to the architecture of Class Activation Mapping (CAM) [79]. However, the averaging limits the extent to which the final visualization depicts the locations within the image that the model is using to make predictions.

Figure 3 illustrates the fundamental problem: each $\alpha^f \mathbf{A}^f$ subcomponent of the final Grad-CAM attention map must always match the relative magnitudes of the feature map \mathbf{A}^f , and either (a) exactly match the positive-negative pattern of the feature map (when α^f is positive), or (b) invert the positive-negative pattern (when α^f is negative). Rescaling and sign changes of individual elements of the feature map are “blurred out.” In HiResCAM, rescaling and sign changes are preserved, producing more high-resolution attention.

Extending Grad-CAM to 3D Data. Grad-CAM was originally described for 2D data [58]. Before introducing the HiResCAM formulation, we describe the extension of Grad-CAM to 3D data.

Recall that s_m is the model’s score for abnormality m before the sigmoid function (equation 1). To obtain a Grad-CAM attention map for abnormality m , we first compute the gradient of s_m with respect to a collection of feature maps $\mathbf{A} = \{\mathbf{A}^f\}_{f=1}^F$ produced by a convolutional layer. For volumetric data, this gradient $\frac{\partial s_m}{\partial \mathbf{A}}$ is 4-dimensional $[F, H, D_1, D_2]$.

Next we calculate a vector of importance weights [58] $\alpha_m \in \mathbb{R}^F$ that will be used to re-weight each corresponding

feature map \mathbf{A}^f . The importance weights are obtained by global average pooling the gradient over the height, width, and depth dimensions:

$$\alpha_m^f = \frac{1}{HD_1D_2} \sum_{h=1}^H \sum_{d_1=1}^{D_1} \sum_{d_2=1}^{D_2} \frac{\partial s_m}{\partial \mathbf{A}_{hd_1d_2}^f}. \quad (3)$$

The importance weights indicate which features are most relevant to this particular abnormality throughout the volume overall. The Grad-CAM attention map is produced as an importance-weighted combination of the feature maps \mathbf{A}^f :

$$\tilde{\mathcal{A}}_m^{\text{GradCAM}} = \sum_{f=1}^F \alpha_m^f \mathbf{A}^f. \quad (4)$$

Following standard practice for use of Grad-CAM [58], the attention map is then post-processed for better visualization by applying a ReLU and normalizing the attention values to the range $[0, 1]$. This step ensures that the regions positively associated with an abnormality will be easily visible.

HiResCAM Formulation. HiResCAM overcomes the limitation of Grad-CAM illustrated in Figure 3. The first step of HiResCAM is the same as the first step of Grad-CAM: compute $\frac{\partial s_m}{\partial \mathbf{A}}$, the gradient of s_m with respect to the feature maps \mathbf{A} .

In the second step of HiResCAM, the attention map is produced by element-wise multiplying the gradient and the feature maps before summing over the feature dimension:

$$\tilde{\mathcal{A}}_m^{\text{HiResCAM}} = \sum_{f=1}^F \frac{\partial s_m}{\partial \mathbf{A}^f} \odot \mathbf{A}^f. \quad (5)$$

The motivation behind HiResCAM is that if the gradients indicate that some elements of the feature map should be scaled or have their sign inverted, then it is more reflective of what the model is computing to perform these operations, rather than to blur the effect of the gradients across each feature map as is done in Grad-CAM.

3.4. HiResCAM intuition: visualizing important image regions

For the most interpretable explanation, HiResCAM should be applied at the last convolutional layer of a CNN that ends in one fully connected layer. In this setup HiResCAM has an intuitive interpretation: the resulting attention map highlights all *locations* within the image that increase the prediction score. In contrast, Grad-CAM emphasizes the *features* that increase the prediction score, which can result in substantially different explanations.

AxialNet enables the optimally interpretable use of HiResCAM, because AxialNet is composed of convolutional layers followed by one fully connected layer. In AxialNet we apply HiResCAM at \mathbf{Z} , the output of the last convolutional layer. In other words, we choose $\mathbf{Z} = \{\mathbf{Z}^f\}_{f=1}^F$

to be our collection of feature maps $\mathbf{A} = \{\mathbf{A}^f\}_{f=1}^F$ and our HiResCAM equation (17) becomes:

$$\tilde{\mathcal{A}}_m^{\text{HiResCAM}} = \sum_{f=1}^F \frac{\partial s_m}{\partial \mathbf{Z}^f} \odot \mathbf{Z}^f. \quad (6)$$

The first step of HiResCAM is thus to calculate $\frac{\partial s_m}{\partial \mathbf{Z}}$, the gradient of the abnormality score s_m with respect to \mathbf{Z} . The previous expression for the abnormality score, $s_m = \frac{1}{H} \sum_{h=1}^H \mathbf{w}_m \mathbf{z}_h + b_m$ (equation 1), described the score in terms of the slice representations \mathbf{z}_h . To rewrite the score s_m in terms of \mathbf{Z} overall requires two concatenations. First, define \mathbf{Z} as the vector resulting from concatenation of all the flattened \mathbf{z}_h representations, $\mathbf{Z} = \mathbf{z}_1 \parallel \mathbf{z}_2 \parallel \dots \parallel \mathbf{z}_H$. Next, define $\mathbf{w}_m^{\text{cat}}$ as the vector resulting from concatenation of the m^{th} -abnormality-specific weights \mathbf{w}_m with themselves H times: $\mathbf{w}_m^{\text{cat}} = \mathbf{w}_m \parallel \mathbf{w}_m \parallel \dots \parallel \mathbf{w}_m$.² Then an alternative expression for the whole volume abnormality score s_m is:

$$s_m = \frac{1}{H} \mathbf{w}_m^{\text{cat}} \mathbf{Z} + b_m. \quad (7)$$

The gradient of the abnormality score s_m with respect to \mathbf{Z} can then be calculated as:

$$\frac{\partial s_m}{\partial \mathbf{Z}} = \frac{\partial}{\partial \mathbf{Z}} \left(\frac{1}{H} \mathbf{w}_m^{\text{cat}} \mathbf{Z} + b_m \right) \quad (8)$$

$$= \frac{1}{H} \mathbf{w}_m^{\text{cat}}. \quad (9)$$

Substituting equation (9) for $\frac{\partial s_m}{\partial \mathbf{Z}}$ into equation 6, we obtain

$$\tilde{\mathcal{A}}_m^{\text{HiResCAM}} = \sum_{f=1}^F \frac{1}{H} \mathbf{w}_m^{\text{cat}} \odot \mathbf{Z}. \quad (10)$$

The element-wise multiplication $\mathbf{w}_m^{\text{cat}} \odot \mathbf{Z}$ in the HiResCAM attention map expression is the intermediate computation in calculating $\mathbf{w}_m^{\text{cat}} \mathbf{Z}$, which in turn is a direct contributor to the abnormality score $s_m = \frac{1}{H} \mathbf{w}_m^{\text{cat}} \mathbf{Z} + b_m$.

Therefore, the large positive elements of the HiResCAM attention map $\tilde{\mathcal{A}}_m$ that show up as abnormality-relevant image locations correspond to locations which directly increase the abnormality score. Similarly, negative elements of the HiResCAM attention map are direct contributors to a lower abnormality score. That means the HiResCAM attention map can be interpreted as showing exactly which parts of the scan contributed most to the abnormality score.

Grad-CAM intuition: visualizing features, not locations. Grad-CAM does not directly visualize important locations. The intuitive interpretation of HiResCAM does not apply, even if Grad-CAM is used at the last convolutional

²Dimensions: $\mathbf{w}_m \in \mathbb{R}^{1 \times F D_1 D_2}$, $b_m \in \mathbb{R}$, $\mathbf{w}_m^{\text{cat}} \in \mathbb{R}^{1 \times H F D_1 D_2}$, and flattened $\mathbf{Z} \in \mathbb{R}^{H F D_1 D_2 \times 1}$.

layer. To calculate the Grad-CAM explanation at the level of \mathbf{Z} , we first follow equation (3) to obtain the importance weights:

$$\alpha_m^f = \frac{1}{HD_1D_2} \sum_{h=1}^H \sum_{d_1=1}^{D_1} \sum_{d_2=1}^{D_2} \frac{1}{H} \mathbf{w}_m^{f^{cat}}. \quad (11)$$

These importance weights are then multiplied against the corresponding feature maps of \mathbf{Z} . Essentially this means that all the fully connected layer weights corresponding to a given feature map are averaged together and then the resulting scalar is multiplied against the feature map. The overall effect is to emphasize the *features* that contribute most to the prediction across the entire image, even if in the model’s computations these important features are only actually contributing to the score in a few focal areas.

Thus, while HiResCAM produces explanations based on the most important image *locations*, Grad-CAM produces explanations based on the most important image *features*. Important features and important locations can coincide, but do not always coincide. We will show that HiResCAM outperforms Grad-CAM at correct abnormality localization in CT scans.

HiResCAM: faithful, computationally efficient label-specific explanations The preceding analysis demonstrated HiResCAM’s relationship to Grad-CAM. HiResCAM is also related to Gradient * Input, thus providing a conceptual link between Grad-CAM and Gradient * Input. If HiResCAM were to be applied at the level of the input image, it would be equivalent to Gradient * Input. While the “level of application” is a simple distinction, it has several critical implications that, to the best of our knowledge, have not been explored previously in the literature. First, HiResCAM explanations are clean and class-specific, whereas Gradient * Input and other pixel-space explanations produce visualizations that are too noisy to be class-specific [58]. Second, HiResCAM is not susceptible to the same issue that caused Gradient * Input to fail basic sanity checks [1]: namely, HiResCAM does not involve element-wise multiplication with the raw input image. Third, when HiResCAM is used as recommended in the previous section, the HiResCAM explanations can be seamlessly integrated into model training in a computationally efficient manner, a consideration that is particularly important when working with massive CT volumes. Equation (10) can be calculated during the forward pass, meaning that no extra backward passes are needed. Finally, because the HiResCAM explanation is in a low-dimensional space, computing a loss on it (Section 3.5) requires orders of magnitude fewer computations than if the same loss were calculated in input space.

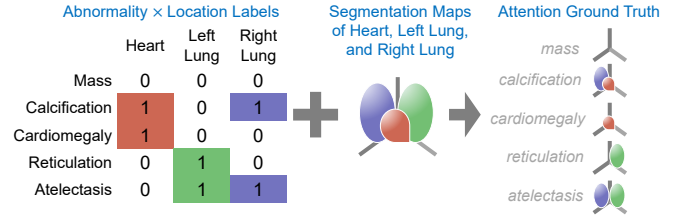


Figure 4. Schematic of the attention ground truth creation via PARTITION. By combining the location \times abnormality labels and the organ segmentation masks, it is possible to define “allowed regions” for each abnormality with no manual labor.

3.5. Proposed mask loss

We propose a mask loss that leverages HiResCAM to improve the quality of explanations by restricting the abnormality-specific attention to allowed regions for each abnormality m . Given the model’s predicted attention $\tilde{\mathcal{A}} \in \mathbb{R}^{M \times H \times D_1 \times D_2}$ and a binary mask $\mathcal{G}_{true} \in \{0, 1\}^{M \times H \times D_1 \times D_2}$ which defines an allowed region for the attention for each abnormality, the mask loss is calculated as follows (using \tilde{a}_i to access all MHD_1D_2 elements of $\tilde{\mathcal{A}}$):

$$\mathcal{L}_{mask} = - \sum_{i: \mathcal{G}_{true}=0} \log(1 - \tilde{a}_i). \quad (12)$$

The proposed mask loss is conceptually half of a segmentation loss [34], applied in a low-dimensional space. To minimize the mask loss the model must not increase the abnormality score using forbidden regions. Further justification for this choice of mask loss is provided in the Supplement. To understand the effect of the mask loss, we train one AxialNet model on the classification loss alone, \mathcal{L}_{class} (equation 2), and another AxialNet model on the overall proposed loss that incorporates both the classification loss and the mask loss: $\mathcal{L}_{total} = \mathcal{L}_{class} + \lambda \mathcal{L}_{mask}$, where λ is a hyperparameter. We found $\lambda = \frac{1}{3}$ to be an effective value.

3.6. PARTITION: Creating an attention ground truth.

The primary barrier to computing the mask loss is obtaining \mathcal{G}_{true} which specifies the allowed regions for each abnormality. Manually creating \mathcal{G}_{true} would require months of expert manual labor. Therefore, we develop PARTITION (“Per Abnormality oRgan masks To guIde aT-tention”), an efficient approach for obtaining \mathcal{G}_{true} computationally. First, we expand the previously described SARLE [20] natural language processing method with location vocabulary, in order to automatically identify the location of each abnormality in the free text CT reports. Next, we develop an unsupervised multi-organ segmenta-

tion pipeline using morphological image processing to define segmentation maps of the right lung, left lung, and heart/mediastinum in each volume individually. The combination of the location \times abnormality labels and the organ segmentation masks enables determination of an “allowed region” for each abnormality as illustrated in Figure 4.

4. Experiments

Datasets. RAD-ChestCT [20] is a data set of 36,316 CT volumes with 83 whole-volume abnormality labels. We focus on $M = 80$ labels relevant to the lungs and heart/mediastinum, detailed in the Supplement. To quantify the effect of HiResCAM and the mask loss on explanation quality, we train and evaluate AxialNet with and without the mask loss using the full data set of 36,316 volumes (> 5 terabytes). For architecture comparisons and ablation studies we use a predefined subset [20] of 2,000 training scans and 1,000 validation scans intended for this purpose, as using the full data set would require > 1 week per comparison.

PASCAL VOC 2012 [22] is a data set of 2D RGB natural images with segmentation maps of 20 classes. Following prior work [70], we combine PASCAL VOC 2012 with SBD [28] to create an augmented training set of 7,087 images. We only use whole-image labels to train classification models.

Implementation details. The per-slice CNN in AxialNet consists of a 2D ResNet-18 [30] pretrained on ImageNet [17] and refined during training on CTs, followed by custom convolutional layers. All models are implemented in PyTorch. Models were trained using stochastic gradient descent with momentum 0.99 and learning rate 10^{-3} . Whole-dataset models were trained on an NVIDIA Tesla V100 GPU with 32 GiB of memory. All code will be made publicly available.

OrganIoU: a metric for explanation quality. There is no standard method to evaluate the quality of a neural network explanation [4]. Weakly supervised segmentation methods are often evaluated with intersection over union (IoU), which requires ground truth class-specific segmentation masks that are not available in any multilabel volumetric medical imaging data set. Therefore we propose OrganIoU, a metric that equals 1 when the model has assigned all abnormality attention within the allowed regions for that abnormality, and equals 0 when the model has only assigned attention to forbidden regions. The OrganIoU is calculated using the model’s predicted attention $\hat{\mathcal{A}} \in \mathbb{R}^{M \times H \times D_1 \times D_2}$ and the attention ground truth $\mathcal{G}_{true} \in \{0, 1\}^{M \times H \times D_1 \times D_2}$. The predicted attention is binarized with different thresholds and the optimal threshold chosen for each abnormality on the validation set. Define *allowed* as the sum of all predicted attention values where $\mathcal{G}_{true} = 1$ and *forbidden* as the sum of all predicted attention values where $\mathcal{G}_{true} = 0$. Then $\text{OrganIoU} = \frac{\text{allowed}}{\text{allowed} + \text{forbidden}}$.

Architecture Comparison and Ablation Study

Model		AUROC	OrganIoU	
			Grad	HiRes
Alternative Architectures	CTNet [20]	66.3	-	-
	3DConv [20]	53.8	3.3	4.5
	BodyConv [20]	50.2	0.0	14.6
	BodyCAM	62.0	15.7	15.7
AxialNet	MaxPool	65.5	9.3	10.9
Ablation	RandInitResNet	63.1	15.1	14.1
Study	NoCustomConv	56.5	10.0	19.7
Proposed	AxialNet	67.5	18.7	21.5

Table 1. Validation set classification performance (median AUROC) and localization performance (mean OrganIoU) using the predefined 2,000 train/1,000 val subset [20] for computational feasibility. The proposed AxialNet architecture outperforms all previously published multilabel CT scan classifiers (CTNet, 3DConv based on 3D convolutions, and BodyConv), as well as a new BodyCAM architecture detailed in the Supplement and ablated versions of AxialNet. OrganIoU was calculated at the last convolutional layer of all models. No OrganIoU could be calculated for CTNet as the spatial relationship between the output of the last convolutional layer and the input has been disrupted due to convolution over features.

AxialNet Test OrganIoU on Whole RAD-ChestCT Dataset

AxialNet \mathcal{L}_{class}		AxialNet $\mathcal{L}_{class} + \lambda \mathcal{L}_{mask}$		Overall
Grad-CAM	HiResCAM	Grad-CAM	HiResCAM	↑
20.1	20.7	21.4	27.6	+37.2%

Table 2. The proposed mask loss and HiResCAM attention mechanism have a synergistic effect that yields state-of-the-art performance with a 37% improvement in explanation quality (20.1 \rightarrow 27.6 OrganIoU). Test set results for two models trained on the whole RAD-ChestCT data set of 36,316 CT volumes: (AxialNet \mathcal{L}_{class} only), vs. (AxialNet $\mathcal{L}_{class} + \lambda \mathcal{L}_{mask}$).

The proposed AxialNet architecture outperforms all previously reported multilabel CT scan classification architectures on both classification and localization (Table 1).

The ablation study on AxialNet emphasizes the benefit of average pooling (vs. MaxPool), use of a pretrained ResNet (vs. RandInitResNet), and inclusion of the custom convolution layers (vs. NoCustomConv) (Table 1).

The proposed HiResCAM attention mechanism outperforms Grad-CAM. HiResCAM yields better abnormality localization than GradCAM overall (Table 2). Recall that both HiResCAM and GradCAM visualizations are calculated *after* the model is finished training; therefore, HiResCAM’s advantage over GradCAM occurs without changing any of the model’s parameters.

HiResCAM faithfully represents where the model is looking, while GradCAM sometimes creates the impression that the model has focused on the wrong organ. Figure 5 includes examples for which Grad-CAM created the

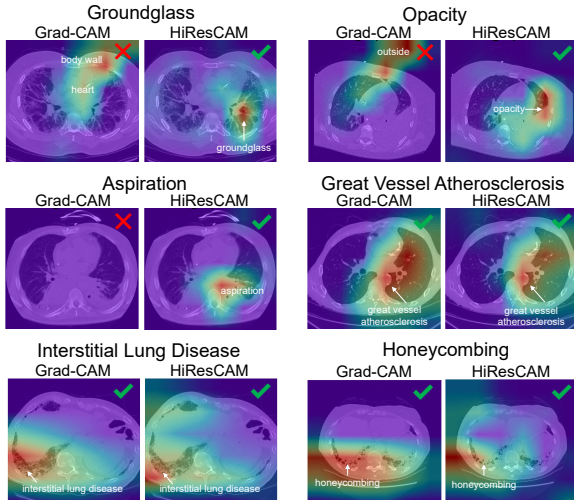


Figure 5. A comparison of Grad-CAM and HiResCAM explanations for true positive predictions of AxialNet $\mathcal{L}_{class} + \lambda\mathcal{L}_{mask}$ trained on the whole RAD-ChestCT data set. For groundglass, opacity, and aspiration, the feature-focused Grad-CAM explanation creates the incorrect impression that the model has made a prediction for a lung abnormality based on the wrong anatomical region, while the location-focused HiResCAM explanations highlight the lung locations that the model actually used. For great vessel atherosclerosis, interstitial lung disease, and honeycombing, both Grad-CAM and HiResCAM produced reasonable results. The fact that Grad-CAM can sometimes highlight the appropriate structure may explain its popularity in medical imaging.

incorrect impression that the model made predictions for lung abnormalities based on the heart or body wall, when in fact the model did rely on the lungs as illustrated in the HiResCAM explanations. We hypothesize that Grad-CAM focuses on the wrong organ because these lung abnormalities are “light grey” and may activate features that detect this “light grey” quality; however, the heart is more “light grey” than any adjacent lung tissue, so feature-focused Grad-CAM fixates incorrectly on the heart. Numerous qualitative results were discussed with a board-certified chest radiologist who agreed that HiResCAM produced better explanations.

HiResCAM reveals when the model behaves incorrectly. We visualized HiResCAM attention maps for 212 incorrect predictions and found that 79% of the maps were sufficient to show that the model was incorrect, due to focus outside the body or on an obviously incorrect organ. The remaining maps enabled quick verification of the abnormality’s true status. **HiResCAM also demonstrates when a model is undesirably exploiting correlations.** In the Supplement we provide a detailed case study of great vessel atherosclerosis, in which HiResCAM illustrates that AxialNet \mathcal{L}_{class} exploited the correlation between atherosclerosis and body wall fat.

The proposed mask loss improves performance. Ta-

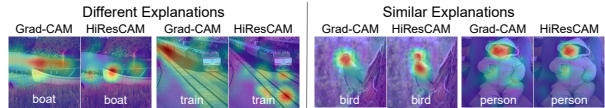


Figure 6. Grad-CAM and HiResCAM explanations for a VGG-16 classifier trained on PASCAL VOC 2012. For the “train” image Grad-CAM highlights the train, while HiResCAM reveals that the model was exploiting a correlation and the tracks were unfortunately the object of focus.

ble 2 demonstrates the benefit of the mask loss, which leverages HiResCAM and PARTITION. The mask loss leads to better OrganIOU for both Grad-CAM and HiResCAM explanation approaches. Analyses of PARTITION’s subcomponents, the location extraction from reports and the organ segmentation, are provided in the Supplement.

The mask loss and HiResCAM synergistically improve performance. The mask loss and HiResCAM together have a synergistic effect that produces state-of-the-art performance, with a 37% improvement (20.1 \rightarrow 27.6 OrganIoU) in explanation quality overall (Table 2).

HiResCAM vs. Grad-CAM in natural images. Experiments on PASCAL VOC 2012 (Figure 6) support the observation that location-focused HiResCAM explanations differ from feature-focused GradCAM explanations. HiResCAM provides insight into key regions. The Supplement includes additional examples.

Future work. It would be interesting to conduct an extensive user study with multiple radiologists evaluating explanations from Grad-CAM and HiResCAM. Furthermore, classification CNNs tend to focus on small discriminative regions [43, 44, 12, 38], causing some explanations to highlight only one example of an abnormality (e.g. bilateral groundglass highlighted on only one side). Exploring methods to capture all regions relevant to an abnormality, without the attention spreading to incorrect organs, is a promising direction for future work.

5. Conclusion

We identify a previously unrecognized limitation of GradCAM: sometimes GradCAM creates the false impression that the model has focused on the wrong organ. We solve this problem with HiResCAM, a label-specific, region-focused attention mechanism that highlights the locations that contribute most to each prediction. We further propose PARTITION, an approach to obtain allowed regions, and a mask loss that leverages HiResCAM and PARTITION to encourage the model to predict abnormalities from only the organs in which they appear. Overall, our innovations result in a 37% improvement in explanation quality, demonstrating state-of-the-art performance on explainable multiple abnormality prediction in 3D medical images.

Acknowledgements. The authors would like to thank the Duke Protected Analytics Computing Environment (PACE), particularly Mike Newton and Charley Kneifel, PhD, for providing the computing resources and GPUs needed to complete this work. The authors also thank Paidamoyo Chapfuwa, MS, for thoughtful comments on the manuscript, David Dov, PhD, for discussion of multiple instance learning, and Geoffrey D. Rubin, MD, FACR, for feedback on the quality of the attention maps.

References

- [1] Julius Adebayo, Justin Gilmer, Michael Muelly, Ian Goodfellow, Moritz Hardt, and Been Kim. Sanity checks for saliency maps. In *Advances in Neural Information Processing Systems*, pages 9505–9515, 2018. [3](#), [6](#)
- [2] Jiwoon Ahn and Suha Kwak. Learning pixel-level semantic affinity with image-level supervision for weakly supervised semantic segmentation. In *Proceedings of the IEEE Conference on Computer Vision and Pattern Recognition*, pages 4981–4990, 2018. [3](#)
- [3] Alan Alexander, Adam Jiang, Cara Ferreira, and Delphine Zurkiya. An intelligent future for medical imaging: a market outlook on artificial intelligence for medical imaging. *Journal of the American College of Radiology*, 17(1):165–170, 2020. [1](#)
- [4] Marco Ancona, Enea Ceolini, Cengiz Öztireli, and Markus Gross. Gradient-based attribution methods. In *Explainable AI: Interpreting, Explaining and Visualizing Deep Learning*, pages 169–191. Springer, 2019. [1](#), [2](#), [7](#), [14](#)
- [5] Marios Anthimopoulos, Stergios Christodoulidis, Lukas Ebner, Andreas Christe, and Stavroula Mougiakakou. Lung pattern classification for interstitial lung diseases using a deep convolutional neural network. *IEEE transactions on medical imaging*, 35(5):1207–1216, 2016. [2](#), [15](#)
- [6] Diego Ardila, Atilla P Kiraly, Sujeeth Bharadwaj, Bokyung Choi, Joshua J Reicher, Lily Peng, Daniel Tse, Mozziyar Etemadi, Wenxing Ye, Greg Corrado, et al. End-to-end lung cancer screening with three-dimensional deep learning on low-dose chest computed tomography. *Nature medicine*, 25(6):954–961, 2019. [2](#)
- [7] Sebastian Bach, Alexander Binder, Grégoire Montavon, Frederick Klauschen, Klaus-Robert Müller, and Wojciech Samek. On pixel-wise explanations for non-linear classifier decisions by layer-wise relevance propagation. *PloS one*, 10(7):e0130140, 2015. [2](#), [14](#)
- [8] David Balduzzi, Marcus Frean, Lennox Leary, JP Lewis, Kurt Wan-Duo Ma, and Brian McWilliams. The shattered gradients problem: If resnets are the answer, then what is the question? *arXiv preprint arXiv:1702.08591*, 2017. [2](#), [14](#)
- [9] Ivo M Baltruschat, Hannes Nickisch, Michael Grass, Tobias Knopp, and Axel Saalbach. Comparison of deep learning approaches for multi-label chest x-ray classification. *Scientific reports*, 9(1):1–10, 2019. [3](#), [15](#)
- [10] David Bermejo-Peláez, Samuel Y Ash, George R Washko, Raúl San José Estépar, and María J Ledesma-Carbayo. Classification of interstitial lung abnormality patterns with an ensemble of deep convolutional neural networks. *Scientific reports*, 10(1):1–15, 2020. [2](#), [15](#)
- [11] Yu-Ting Chang, Qiaosong Wang, Wei-Chih Hung, Robinson Piramuthu, Yi-Hsuan Tsai, and Ming-Hsuan Yang. Mixupcam: Weakly-supervised semantic segmentation via uncertainty regularization. *arXiv preprint arXiv:2008.01201*, 2020. [3](#), [16](#)
- [12] Yu-Ting Chang, Qiaosong Wang, Wei-Chih Hung, Robinson Piramuthu, Yi-Hsuan Tsai, and Ming-Hsuan Yang. Weakly-supervised semantic segmentation via sub-category exploration. In *Proceedings of the IEEE/CVF Conference on Computer Vision and Pattern Recognition*, pages 8991–9000, 2020. [3](#), [8](#), [16](#)
- [13] Stergios Christodoulidis, Marios Anthimopoulos, Lukas Ebner, Andreas Christe, and Stavroula Mougiakakou. Multi-source transfer learning with convolutional neural networks for lung pattern analysis. *IEEE journal of biomedical and health informatics*, 21(1):76–84, 2016. [2](#), [15](#)
- [14] K Clark, B Vendt, K Smith, J Freymann, J Kirby, P Koppel, S Moore, S Phillips, D Maffitt, M Pringle, L Tarbox, and F Prior. The cancer imaging archive (tcia): Maintaining and operating a public information repository. *Journal of Digital Imaging*, 26(6):1045–1057, 2013. [18](#)
- [15] Diana Crossley, Mary Renton, Muhammad Khan, Emma V Low, and Alice M Turner. Ct densitometry in emphysema: a systematic review of its clinical utility. *International journal of chronic obstructive pulmonary disease*, 13:547, 2018. [2](#)
- [16] Pim A de Jong, Willem E Hellings, Richard AP Takx, Ivana Išgum, Joost A van Herwaarden, and P Th M Willem. Computed tomography of aortic wall calcifications in aortic dissection patients. *PloS one*, 9(7):e102036, 2014. [18](#)
- [17] Jia Deng, Wei Dong, Richard Socher, Li-Jia Li, Kai Li, and Li Fei-Fei. Imagenet: A large-scale hierarchical image database. In *2009 IEEE conference on computer vision and pattern recognition*, pages 248–255. Ieee, 2009. [7](#)
- [18] Ashis Kumar Dhara, Sudipta Mukhopadhyay, Anirvan Dutta, Mandeep Garg, and Niranjana Khandelwal. A combination of shape and texture features for classification of pulmonary nodules in lung ct images. *Journal of digital imaging*, 29(4):466–475, 2016. [2](#)
- [19] Qi Dou, Cheng Chen, Cheng Ouyang, Hao Chen, and Pheng Ann Heng. Unsupervised domain adaptation of convnets for medical image segmentation via adversarial learning. In *Deep Learning and Convolutional Neural Networks for Medical Imaging and Clinical Informatics*, pages 93–115. Springer, 2019. [18](#)
- [20] Rachel Lea Draelos, David Dov, Maciej A. Mazurowski, Joseph Y. Lo, Ricardo Henao, Geoffrey D. Rubin, and Lawrence Carin. Machine-learning-based multiple abnormality prediction with large-scale chest computed tomography volumes. *Medical Image Analysis*, 67, 2021. [2](#), [4](#), [6](#), [7](#), [17](#), [18](#), [20](#)
- [21] Rachael M Edwards, J David Godwin, Dan S Hippe, and Gregory Kicska. A quantitative approach to distinguish pneumonia from atelectasis using computed tomography attenuation. *Journal of computer assisted tomography*, 40(5):746–751, 2016. [2](#)

- [22] Mark Everingham, Luc Van Gool, Christopher KI Williams, John Winn, and Andrew Zisserman. The pascal visual object classes (voc) challenge. *International journal of computer vision*, 88(2):303–338, 2010. **7**
- [23] Junsong Fan, Zhaoxiang Zhang, Chunfeng Song, and Tieniu Tan. Learning integral objects with intra-class discriminator for weakly-supervised semantic segmentation. In *Proceedings of the IEEE/CVF Conference on Computer Vision and Pattern Recognition*, pages 4283–4292, 2020. **3**
- [24] Junsong Fan, Zhaoxiang Zhang, Tieniu Tan, Chunfeng Song, and Jun Xiao. Cian: Cross-image affinity net for weakly supervised semantic segmentation. In *Proceedings of the AAAI Conference on Artificial Intelligence*, volume 34, pages 10762–10769, 2020. **3**
- [25] T Franquet. Imaging of pneumonia: trends and algorithms. *European Respiratory Journal*, 18(1):196–208, 2001. **2**
- [26] Mingchen Gao, Ulas Bagci, Le Lu, Aaron Wu, Mario Buty, Hoo-Chang Shin, Holger Roth, Georgios Z Papadakis, Adrien Depeursinge, Ronald M Summers, et al. Holistic classification of ct attenuation patterns for interstitial lung diseases via deep convolutional neural networks. *Computer Methods in Biomechanics and Biomedical Engineering: Imaging & Visualization*, 6(1):1–6, 2018. **2, 15**
- [27] Mingchen Gao, Ziyue Xu, Le Lu, Adam P Harrison, Ronald M Summers, and Daniel J Mollura. Multi-label deep regression and unordered pooling for holistic interstitial lung disease pattern detection. In *International Workshop on Machine Learning in Medical Imaging*, pages 147–155. Springer, 2016. **2, 15**
- [28] Bharath Hariharan, Pablo Arbeláez, Lubomir Bourdev, Subhransu Maji, and Jitendra Malik. Semantic contours from inverse detectors. In *2011 International Conference on Computer Vision*, pages 991–998. IEEE, 2011. **7**
- [29] Tamara Miner Haygood, Patrick C Brennan, John Ryan, Jose-Miguel Yamal, Lindsay Liles, Paul O’Sullivan, Colleen M Costelloe, Nancy E Fitzgerald, and William A Murphy Jr. Central venous line placement in the superior vena cava and the azygos vein: differentiation on posteroanterior chest radiographs. *American Journal of Roentgenology*, 196(4):783–787, 2011. **18**
- [30] Kaiming He, Xiangyu Zhang, Shaoqing Ren, and Jian Sun. Deep residual learning for image recognition. In *Proceedings of the IEEE conference on computer vision and pattern recognition*, pages 770–778, 2016. **7, 14**
- [31] Gao Huang, Zhuang Liu, Laurens Van Der Maaten, and Kilian Q Weinberger. Densely connected convolutional networks. In *Proceedings of the IEEE conference on computer vision and pattern recognition*, pages 4700–4708, 2017. **14**
- [32] Zilong Huang, Xinggong Wang, Jiasi Wang, Wenyu Liu, and Jingdong Wang. Weakly-supervised semantic segmentation network with deep seeded region growing. In *Proceedings of the IEEE Conference on Computer Vision and Pattern Recognition*, pages 7014–7023, 2018. **3**
- [33] Stephen M Humphries, Aleena M Notary, Juan Pablo Centeno, Matthew J Strand, James D Crapo, Edwin K Silverman, David A Lynch, and Genetic Epidemiology of COPD (COPDGene) Investigators. Deep learning enables automatic classification of emphysema pattern at ct. *Radiology*, 294(2):434–444, 2020. **2**
- [34] Shruti Jadon. A survey of loss functions for semantic segmentation. *arXiv preprint arXiv:2006.14822*, 2020. **6, 17**
- [35] Peng-Tao Jiang, Qibin Hou, Yang Cao, Ming-Ming Cheng, Yunchao Wei, and Hong-Kai Xiong. Integral object mining via online attention accumulation. In *Proceedings of the IEEE International Conference on Computer Vision*, pages 2070–2079, 2019. **3**
- [36] Sanhyun Jo and In-Jae Yu. Puzzle-cam: Improved localization via matching partial and full features. *arXiv preprint arXiv:2101.11253*, 2021. **16**
- [37] Ali Nawaz Khan, Hamdan H Al-Jahdali, Carolyn M Allen, Klaus L Irion, Sarah Al Ghanem, and Shyam Sunder Koteyar. The calcified lung nodule: what does it mean? *Annals of thoracic medicine*, 5(2):67, 2010. **18**
- [38] Alexander Kolesnikov and Christoph H Lampert. Seed, expand and constrain: Three principles for weakly-supervised image segmentation. In *European conference on computer vision*, pages 695–711. Springer, 2016. **3, 8**
- [39] Hsuan-Chang Kuo, Ying-Jui Lin, Chien-Fu Huang, Shao-Ju Chien, I-Chun Lin, Mao-Hung Lo, and Chi-Di Liang. Small-bore pigtail catheters for the treatment of primary spontaneous pneumothorax in young adolescents. *Emergency Medicine Journal*, 30(3):e17–e17, 2013. **18**
- [40] Sebastian Lapuschkin, Alexander Binder, Grégoire Montavon, Klaus-Robert Müller, and Wojciech Samek. Analyzing classifiers: Fisher vectors and deep neural networks. In *Proceedings of the IEEE Conference on Computer Vision and Pattern Recognition*, pages 2912–2920, 2016. **1**
- [41] Sebastian Lapuschkin, Stephan Wäldchen, Alexander Binder, Grégoire Montavon, Wojciech Samek, and Klaus-Robert Müller. Unmasking clever hans predictors and assessing what machines really learn. *Nature communications*, 10(1):1–8, 2019. **1**
- [42] Hyunkwang Lee, Sehyo Yune, Mohammad Mansouri, Myeongchan Kim, Shahein H Tajmir, Claude E Guerrier, Sarah A Ebert, Stuart R Pomerantz, Javier M Romero, Shahmir Kamalian, et al. An explainable deep-learning algorithm for the detection of acute intracranial haemorrhage from small datasets. *Nature Biomedical Engineering*, 3(3):173, 2019. **3, 15**
- [43] Jungbeom Lee, Eunji Kim, Sungmin Lee, Jangho Lee, and Sungroh Yoon. Ficklenet: Weakly and semi-supervised semantic image segmentation using stochastic inference. In *Proceedings of the IEEE conference on computer vision and pattern recognition*, pages 5267–5276, 2019. **3, 8, 16**
- [44] Kunpeng Li, Ziyang Wu, Kuan-Chuan Peng, Jan Ernst, and Yun Fu. Tell me where to look: Guided attention inference network. In *Proceedings of the IEEE Conference on Computer Vision and Pattern Recognition*, pages 9215–9223, 2018. **3, 8, 16**
- [45] Lin Li, Lixin Qin, Zeguo Xu, Youbing Yin, Xin Wang, Bin Kong, Junjie Bai, Yi Lu, Zhenghan Fang, Qi Song, et al. Using artificial intelligence to detect covid-19 and community-acquired pneumonia based on pulmonary ct: evaluation of the diagnostic accuracy. *Radiology*, 296(2), 2020. **4**

- [46] Xiang Li, James H Thrall, Subba R Digumarthy, Manudeep K Kalra, Pari V Pandharipande, Bowen Zhang, Chayanin Nitiwarangkul, Ramandeep Singh, Ruhani Doda Khera, and Quanzheng Li. Deep learning-enabled system for rapid pneumothorax screening on chest ct. *European journal of radiology*, 120:108692, 2019. [2](#)
- [47] Zhan Wei Lim, Mong Li Lee, Wynne Hsu, and Tien Yin Wong. Building trust in deep learning system towards automated disease detection. In *Proceedings of the AAAI Conference on Artificial Intelligence*, volume 33, pages 9516–9521, 2019. [1](#)
- [48] Michael T Lu, Alexander Ivanov, Thomas Mayrhofer, Ahmed Hosny, Hugo JWL Aerts, and Udo Hoffmann. Deep learning to assess long-term mortality from chest radiographs. *JAMA network open*, 2(7):e197416–e197416, 2019. [3](#), [15](#)
- [49] Weili Nie, Yang Zhang, and Ankit Patel. A theoretical explanation for perplexing behaviors of backpropagation-based visualizations. *arXiv preprint arXiv:1805.07039*, 2018. [2](#), [14](#)
- [50] Anastasia Oikonomou and Panos Prassopoulos. Ct imaging of blunt chest trauma. *Insights into imaging*, 2(3):281–295, 2011. [2](#)
- [51] Harsh Panwar, PK Gupta, Mohammad Khubeb Siddiqui, Ruben Morales-Menendez, Prakhar Bhardwaj, and Vaishnavi Singh. A deep learning and grad-cam based color visualization approach for fast detection of covid-19 cases using chest x-ray and ct-scan images. *Chaos, Solitons & Fractals*, 140:110190, 2020. [3](#)
- [52] F Pasa, V Golkov, F Pfeiffer, D Cremers, and D Pfeiffer. Efficient deep network architectures for fast chest x-ray tuberculosis screening and visualization. *Scientific reports*, 9(1):1–9, 2019. [3](#), [15](#)
- [53] Shine Raju, Subha Ghosh, and Atul C Mehta. Chest ct signs in pulmonary disease: a pictorial review. *Chest*, 151(6):1356–1374, 2017. [2](#)
- [54] Marco Tulio Ribeiro, Sameer Singh, and Carlos Guestrin. ” why should i trust you?” explaining the predictions of any classifier. In *Proceedings of the 22nd ACM SIGKDD international conference on knowledge discovery and data mining*, pages 1135–1144, 2016. [1](#)
- [55] Blaine Rister, Kaushik Shivakumar, Tomomi Nobashi, and Daniel Rubin. Ct-org: Ct volumes with multiple organ segmentations dataset. *The Cancer Imaging Archive*, 2019. [18](#)
- [56] Blaine Rister, Darvin Yi, Kaushik Shivakumar, Tomomi Nobashi, and Daniel Rubin. Ct organ segmentation using gpu data augmentation, unsupervised labels and iou loss. *arXiv*, 2018. [18](#)
- [57] Khaled Saab, Jared Dunnmon, Roger Goldman, Alex Ratner, Hersh Sagreiya, Christopher Ré, and Daniel Rubin. Doubly weak supervision of deep learning models for head ct. In *International Conference on Medical Image Computing and Computer-Assisted Intervention*, pages 811–819. Springer, 2019. [4](#)
- [58] Ramprasaath R Selvaraju, Michael Cogswell, Abhishek Das, Ramakrishna Vedantam, Devi Parikh, and Dhruv Batra. Grad-cam: Visual explanations from deep networks via gradient-based localization. In *Proceedings of the IEEE international conference on computer vision*, pages 618–626, 2017. [2](#), [4](#), [5](#), [6](#), [13](#)
- [59] Yan Shen and Mingchen Gao. Dynamic routing on deep neural network for thoracic disease classification and sensitive area localization. In *International Workshop on Machine Learning in Medical Imaging*, pages 389–397. Springer, 2018. [3](#)
- [60] Yiwey Shieh and Martin Bohnenkamp. Low-dose ct scan for lung cancer screening: clinical and coding considerations. *Chest*, 152(1):204–209, 2017. [2](#)
- [61] Avanti Shrikumar, Peyton Greenside, Anna Shcherbina, and Anshul Kundaje. Not just a black box: Learning important features through propagating activation differences. *arXiv preprint arXiv:1605.01713*, 2016. [2](#), [14](#)
- [62] Karen Simonyan, Andrea Vedaldi, and Andrew Zisserman. Deep inside convolutional networks: Visualising image classification models and saliency maps. *ICLR*, 2014. [2](#), [14](#)
- [63] Jost Tobias Springenberg, Alexey Dosovitskiy, Thomas Brox, and Martin Riedmiller. Striving for simplicity: The all convolutional net. *arXiv preprint arXiv:1412.6806*, 2014. [2](#), [14](#)
- [64] Baskaran Sundaram, Barry H Gross, Fernando J Martinez, Eugene Oh, Nestor L Muller, Matt Schipper, and Ella A Kazerooni. Accuracy of high-resolution ct in the diagnosis of diffuse lung disease: effect of predominance and distribution of findings. *American Journal of Roentgenology*, 191(4):1032–1039, 2008. [23](#)
- [65] Christian Szegedy, Wei Liu, Yangqing Jia, Pierre Sermanet, Scott Reed, Dragomir Anguelov, Dumitru Erhan, Vincent Vanhoucke, and Andrew Rabinovich. Going deeper with convolutions. In *Proceedings of the IEEE conference on computer vision and pattern recognition*, pages 1–9, 2015. [14](#)
- [66] Masashi Takahashi, Junya Fukuoka, Norihisa Nitta, Ryutaro Takazakura, Yukihiro Nagatani, Yoko Murakami, Hideji Otani, and Kiyoshi Murata. Imaging of pulmonary emphysema: a pictorial review. *International journal of chronic obstructive pulmonary disease*, 3(2):193, 2008. [23](#)
- [67] Simon LF Walsh, Lucio Calandriello, Mario Silva, and Nicola Sverzellati. Deep learning for classifying fibrotic lung disease on high-resolution computed tomography: a case-cohort study. *The Lancet Respiratory Medicine*, 6(11):837–845, 2018. [2](#), [15](#)
- [68] Chenglong Wang, Takayasu Moriya, Yuichiro Hayashi, Holger Roth, Le Lu, Masahiro Oda, Hiroto Ohkubo, and Kensaku Mori. Weakly-supervised deep learning of interstitial lung disease types on ct images. In *Medical Imaging 2019: Computer-Aided Diagnosis*, volume 10950, page 109501H. International Society for Optics and Photonics, 2019. [2](#), [15](#)
- [69] Xiang Wang, Shaodi You, Xi Li, and Huimin Ma. Weakly-supervised semantic segmentation by iteratively mining common object features. In *Proceedings of the IEEE conference on computer vision and pattern recognition*, pages 1354–1362, 2018. [3](#)
- [70] Yude Wang, Jie Zhang, Meina Kan, Shiguang Shan, and Xilin Chen. Self-supervised equivariant attention mechanism for weakly supervised semantic segmentation. In *Pro-*

ceedings of the IEEE/CVF Conference on Computer Vision and Pattern Recognition, pages 12275–12284, 2020. 3, 7

- [71] Yunchao Wei, Jiashi Feng, Xiaodan Liang, Ming-Ming Cheng, Yao Zhao, and Shuicheng Yan. Object region mining with adversarial erasing: A simple classification to semantic segmentation approach. In *Proceedings of the IEEE conference on computer vision and pattern recognition*, pages 1568–1576, 2017. 3
- [72] Yunchao Wei, Huaxin Xiao, Honghui Shi, Zequn Jie, Jiashi Feng, and Thomas S Huang. Revisiting dilated convolution: A simple approach for weakly- and semi-supervised semantic segmentation. In *Proceedings of the IEEE Conference on Computer Vision and Pattern Recognition*, pages 7268–7277, 2018. 3
- [73] P Whiting, N Singatullina, and JH Rosser. Computed tomography of the chest: I. basic principles. *Bja Education*, 15(6):299–304, 2015. 3
- [74] Jinzhong Yang, Greg Sharp, Harini Veeraraghavan, Wouter van Elmpt, Andre Dekker, Tim Lustberg, and Mark Gooding. Data from lung ct segmentation challenge. *The Cancer Imaging Archive*, 2017. 18
- [75] Jinzhong Yang, Harini Veeraraghavan, Samuel G Armato III, Keyvan Farahani, Justin S Kirby, Jayashree Kalpathy-Kramer, Wouter van Elmpt, Andre Dekker, Xiao Han, Xue Feng, et al. Autosegmentation for thoracic radiation treatment planning: A grand challenge at aapm 2017. *Medical physics*, 45(10):4568–4581, 2018. 18
- [76] Hye Jin Yoo and Kyung Mook Choi. Adipokines as a novel link between obesity and atherosclerosis. *World journal of diabetes*, 5(3):357, 2014. 24
- [77] John R Zech, Marcus A Badgeley, Manway Liu, Anthony B Costa, Joseph J Titano, and Eric Karl Oermann. Variable generalization performance of a deep learning model to detect pneumonia in chest radiographs: a cross-sectional study. *PLoS medicine*, 15(11):e1002683, 2018. 1
- [78] Matthew D Zeiler and Rob Fergus. Visualizing and understanding convolutional networks. In *European conference on computer vision*, pages 818–833. Springer, 2014. 2, 14
- [79] Bolei Zhou, Aditya Khosla, Agata Lapedriza, Aude Oliva, and Antonio Torralba. Learning deep features for discriminative localization. In *Proceedings of the IEEE conference on computer vision and pattern recognition*, pages 2921–2929, 2016. 1, 2, 4, 12, 16

Supplementary Material

The first part of the Supplementary Material focuses on HiResCAM. Section 6 shows that HiResCAM is a generalization of CAM. Section 7 analyzes CAM, Grad-CAM, and HiResCAM in the context of different CNN architectures. Section 8 explains the BodyCAM architecture and illustrates the benefit of the AxialNet approach which preserves spatial information about features in the representation fed in to the final fully connected layer, in contrast to BodyCAM which destroys this information with the global average pooling step. Section 9 illustrates through literature examples how our recommendations for HiResCAM and CNN architectures could benefit explainability in medical imaging applications. Section 10 distinguishes between the goals of gradient-based explanation and weakly-supervised segmentation. Finally, Section 11 connects to an observation made by the authors of the original CAM paper, who pointed out that the biases in the final fully connected layer appeared to have minimal effect on the visualizations; by leveraging the fact that HiResCAM is a generalization of CAM, this section shows why the biases of the final fully connected layer do not affect the visualizations.

In the next part of the Supplementary Material we consider the mask loss, PARTITION, and additional experimental results on RAD-ChestCT and PASCAL VOC 2012. Section 12 provides further justification for the mask loss. Section 13 details the attention ground truth creation with PARTITION and includes a full list of the 80 abnormality labels divided into concept groups (Table 5) as well as qualitative lung segmentation results (Figure 8). Section 14 provides additional results for HiResCAM and Grad-CAM on PASCAL VOC 2012. The last section, Section 15 on RAD-ChestCT, demonstrates that the abnormality scores across slices ($C \in \mathbb{R}^{M \times H}$) reflect medical concepts. This section also includes the great vessel atherosclerosis case study illustrating how the mask loss reduces inappropriate exploitation of confounding variables.

6. HiResCAM is a generalization of CAM

In this section we demonstrate that HiResCAM is a generalization of CAM.

Class Activation Mapping [79], or CAM, is a CNN explanation method that requires a particular architecture: convolutional layers, then global average pooling of feature maps over all spatial dimensions, then a single fully-connected layer. We will henceforth refer to this as the “CAM architecture.” CAM was developed with the observation that for this particular architecture, it is straightforward to visualize the regions of the input image that directly contribute to an increased score for a particular label. In the remainder of the section we will consider a 2D CNN example, without loss of generality to 3D or n D CNNs.

Consider the following 2D ‘‘CAM architecture’’ for an input image \mathbf{X} :

1. Convolutional layers: $\text{conv}(\mathbf{X}) = \{\mathbf{A}\}_{f=1}^F$ where each feature map \mathbf{A}^f is 2-dimensional $[D_1, D_2]$ and was produced by the last convolutional layer.
2. Global average pooling of each feature map to a scalar:

$$a^f = \frac{1}{D_1 D_2} \sum_{d_1=1}^{D_1} \sum_{d_2=1}^{D_2} \mathbf{A}_{d_1 d_2}^f. \quad (13)$$

3. Final fully connected layer:

$$s_m = w_m^1 a^1 + w_m^2 a^2 + \dots + w_m^F a^F \text{ for } m = 1, \dots, M \quad (14)$$

where s_m is the score for the m^{th} class and there are M classes total.

The CAM explanation for class m is then:

$$\tilde{\mathcal{A}}_m^{\text{CAM}} = w_m^1 \mathbf{A}^1 + w_m^2 \mathbf{A}^2 + \dots + w_m^F \mathbf{A}^F, \quad (15)$$

or equivalently:

$$\tilde{\mathcal{A}}_m^{\text{CAM}} = \sum_{f=1}^F w_m^f \mathbf{A}^f. \quad (16)$$

Recall that the formulation for HiResCAM is

$$\tilde{\mathcal{A}}_m^{\text{HiResCAM}} = \sum_{f=1}^F \frac{\partial s_m}{\partial \mathbf{A}^f} \odot \mathbf{A}^f. \quad (17)$$

To calculate the HiResCAM map, we must thus calculate $\frac{\partial s_m}{\partial \mathbf{A}^f}$, the gradient of the score with respect to the feature maps produced by the last convolutional layer.

First we re-write the score s_m in terms of these feature maps, by plugging the right-hand side of the global average pooling equation 13 into the final fully connected layer equation 14:

$$s_m = w_m^1 \left(\frac{1}{D_1 D_2} \sum_{d_1=1}^{D_1} \sum_{d_2=1}^{D_2} \mathbf{A}_{d_1 d_2}^1 \right) \quad (18)$$

$$+ w_m^2 \left(\frac{1}{D_1 D_2} \sum_{d_1=1}^{D_1} \sum_{d_2=1}^{D_2} \mathbf{A}_{d_1 d_2}^2 \right) \quad (19)$$

$$+ \dots + w_m^F \left(\frac{1}{D_1 D_2} \sum_{d_1=1}^{D_1} \sum_{d_2=1}^{D_2} \mathbf{A}_{d_1 d_2}^F \right). \quad (20)$$

From the above expression we can see that the gradient $\frac{\partial s_m}{\partial \mathbf{A}^f}$ is

$$\frac{\partial s_m}{\partial \mathbf{A}^f} = \frac{1}{D_1 D_2} w_m^f, \quad (21)$$

which means that the HiResCAM explanation is:

$$\tilde{\mathcal{A}}_m^{\text{HiResCAM}} = \frac{1}{D_1 D_2} \sum_{f=1}^F w_m^f \mathbf{A}^f. \quad (22)$$

This is identical to the CAM explanation (equation 16) except for a constant factor of $\frac{1}{D_1 D_2}$ which will disappear in the HiResCAM normalization step.

For another perspective, consider that the gradient of the score for class m with respect to the pooling outputs a^1, a^2, \dots, a^F are the respective m -specific weights $w_m^1, w_m^2, \dots, w_m^F$. Each w_m^f value is then propagated back through the global average pooling step by considering how many elements were pooled together, and distributing w_m^f equally across all those elements - that is, dividing w_m^f by $D_1 D_2$, which is the total number of elements in each feature map.

Thus, HiResCAM is a generalization of CAM because both methods yield the same explanation for the ‘‘CAM Architecture’’ but HiResCAM is applicable to a broader class of architectures.

In the Grad-CAM paper [58], the authors show that Grad-CAM is also a generalization of CAM. Thus, HiResCAM and Grad-CAM are alternative generalizations of the CAM method. Grad-CAM was the first work to analyze the relationship between gradients and the CAM method. We build on Grad-CAM by identifying that Grad-CAM’s gradient averaging step produces feature-focused explanations that can sometimes highlight the wrong location. By avoiding the gradient averaging step with HiResCAM, we obtain location-focused explanations that are guaranteed to show the regions the model is using for a particular prediction, an explainability method characteristic that is critical in sensitive applications like medical imaging.

7. Comparing CAM, Grad-CAM, and HiResCAM by architecture

In this section, we provide a detailed comparison of CAM, Grad-CAM, and HiResCAM according to their architecture requirements and guarantees. From specific to general, the architectures we consider are: (1) the ‘‘CAM architecture’’; (2) CNNs ending in only one fully-connected layer; (3) all other CNNs.

7.1. “CAM architecture”: CNNs ending in global average pooling then one fully connected layer

For the “CAM architecture” the following methods produce identical explanations: CAM, Grad-CAM applied at the last convolutional layer, and HiResCAM applied at the last convolutional layer. This is because Grad-CAM and HiResCAM are alternative generalizations of CAM. This explanation is provably guaranteed to highlight only relevant locations. Examples of models that follow the “CAM architecture” include ResNets [30], GoogLeNet [65], and DenseNets [31].

7.2. CNNs ending in only one fully connected layer

For all CNNs that end in one fully connected layer (e.g. AxialNet), the HiResCAM explanation produced at the last convolutional layer is guaranteed to highlight only relevant locations. The same guarantee does *not* hold for Grad-CAM, as shown in the main paper. Without global average pooling before the final fully connected layer, CAM explanations cannot be calculated at all.

7.3. All other CNNs

For all other CNNs, including those ending in multiple fully connected layers, CAM explanations cannot be calculated, and while HiResCAM and Grad-CAM explanations can be calculated, they are not provably guaranteed to highlight only relevant locations. To the best of our knowledge, no neural network explanation method yet exists which can produce class-specific explanations guaranteed to highlight only the regions the model is actually using, for any arbitrary architecture or layer. As discussed in the related work section of the main paper, the gradient-based explanation methods saliency mapping [62], DeconvNets [78], Guided Backpropagation [63], Gradient * Input [61], and LRP [7] can be applied to many architectures, but suffer from the shattered gradients problem [8, 49] which leads to a “white noise” appearance of the final explanation that eliminates class specificity in practice. Nonlinearities present particular challenges for gradient-based explanation methods. Handling of the ReLUs in DeconvNets and Guided Backpropagation leads these methods to perform partial image recovery instead of providing an explanation of what the model is actually doing [49].

For sensitive applications where trustworthy class-specific explanations are required, we recommend using either HiResCAM with a CNN ending in only one fully connected layer, or CAM with a CNN ending in global average pooling and one fully connected layer.

7.4. Connection between HiResCAM, CNNs ending in only one fully connected layer, and regression

Understanding why CNNs ending in only one fully connected layer are most amenable to interpretation can be appreciated through their connection to regression. Ancona *et al.* discuss regression in relation to gradient-based explanation methods in Chapter 9 of “Explainable AI: Interpreting, Explaining, and Visualizing Deep Learning” [4]. In brief, for a simple example $y = w_1x_1 + w_2x_2$, a *global explanation* consists of inspecting the numeric values of the learned coefficients w_1 and w_2 - for example if $w_1 = 1.3$ and $w_2 = -2.2$ then we know that adding 1 to the value of x_1 will increase the prediction by 1.3, while adding 1 to the value of x_2 will decrease the prediction by 2.2. This global explanation is equivalent to the model gradient. A *local explanation* considers the values of w_1x_1 and w_2x_2 to understand the prediction for a particular input example; this local explanation is equivalent to the gradient multiplied element-wise by the input.

A CNN ending in a single fully connected layer is a feature extractor followed by regression. The feature extractor produces a collection of numbers summarizing the input, and this collection of numbers is fed in to the regression to make the final prediction. HiResCAM is the local explanation that demonstrates for a particular example the most important locations for the prediction.

8. The BodyCAM architecture and an advantage of AxialNet

Given the close connection between HiResCAM and CAM, a natural question is how much value HiResCAM adds by eliminating the requirement for global average pooling before the final fully connected layer. We begin to explore this question through the BodyCAM architecture, which is similar to AxialNet except that it obeys the “CAM architecture” constraints. We hypothesized that for CT scan analysis, there would be a benefit to avoiding the global average pooling step in order to preserve the information about spatial locations of certain features - in other words, we hypothesized that AxialNet would outperform BodyCAM. Our experimental results support this hypothesis, with AxialNet achieving better AUROC than BodyCAM as shown in Table 1 of the main paper.

The first part of the BodyCAM model is the same as AxialNet, consisting of a 2D ResNet and custom convolutional layers applied to each slice. However, after this point, the BodyCAM architecture differs from AxialNet’s architecture. After the custom convolutional layers, BodyCAM uses 3D global average pooling over the $[H, D_1, D_2]$ spatial dimensions, and then a fully connected layer produces the final predictions, whereas AxialNet follows a multi-

Paper	Architecture	Is the architecture a “CAM architecture”?	Were results of a visual explanation method reported in the paper?	If a visual explanation method were applied, could it highlight incorrect locations?
An explainable deep-learning algorithm for the detection of acute intracranial haemorrhage from small datasets. [42]	VGG16, ResNet-50, Inception-v3 and Inception-ResNet-v2	No for VGG-16. Yes for ResNet-50, Inception-v3, and Inception-ResNet-v2.	Grad-CAM (paper described it verbally as “CAM” but the equation shown and references indicate it was Grad-CAM)	Yes, at a minimum for the VGG-16 model which ends in >1 FC layer.
Comparison of deep learning approaches for multi-label chest x-ray classification. [9]	ResNet-50	Yes	Grad-CAM was applied at the final convolutional layer of an architecture that follows the “CAM architecture”—thus, this attention approach is mathematically equivalent to CAM	No
Efficient deep network architectures for fast chest x-ray tuberculosis screening and visualization. [52]	Custom CNN ending in global average pooling then one FC layer	Yes	Saliency maps and Grad-CAM were applied at different layers. From the figure appearance, it appears that Guided Grad-CAM was used rather than vanilla Grad-CAM.	Yes, because Grad-CAM was applied at different layers, and also because Guided Grad-CAM appears to have been used.
Deep learning to assess long-term mortality from chest radiographs. [48]	Modified Inception-v4 architecture ending in > 1 FC layer	No	Grad-CAM	Yes, because Grad-CAM was applied to a CNN ending in >1 FC layer.
Classification of Interstitial Lung Abnormality Patterns with an Ensemble of Deep Convolutional Neural Networks [10]	Ensemble of 7 CNNs. Architectures include BCNN, MSTAGE-CNN, and MCONTEXT, which all end in 2 or more FC layers.	No	No	Yes: architectures ending in >1 FC layers were used.
Weakly-supervised deep learning of interstitial lung disease types on CT images [68]	Custom CNN ending in >1 FC layer.	No	No	Yes: an architecture ending in >1 FC layer was used.
Holistic classification of CT attenuation patterns for interstitial lung diseases via deep convolutional neural networks [26]	Custom CNN ending in 3 FC layers.	No	No	Yes: an architecture ending in >1 FC layer was used.
Deep learning for classifying fibrotic lung disease on high-resolution computed tomography: a case-cohort study [67]	Inception-ResNet-v2	Yes	No	No, if CAM or Grad-CAM or HiResCAM was applied at the last convolutional layer.
Multisource Transfer Learning With Convolutional Neural Networks for Lung Pattern Analysis [13]	Custom CNN ending in 3 FC layers.	No	No	Yes: an architecture ending in >1 FC layer was used.
Lung Pattern Classification for Interstitial Lung Diseases Using a Deep Convolutional Neural Network [5]	Custom CNN ending in >1 FC layer	No	No	Yes: an architecture ending in >1 FC layer was used.
Multi-label Deep Regression and Unordered Pooling for Holistic Interstitial Lung Disease Pattern Detection [27]	AlexNet variant ending in 2 FC layers.	No	No	Yes: an architecture ending in >1 FC layer was used.

Table 3. Example studies in medical imaging, particularly CT scan analysis, and assessment of whether a visual explanation method could highlight locations the model did not actually use for prediction. When there is a risk (final column orange), that risk could be removed by using our proposed HiResCAM explanation method coupled with modifying the architecture to end in only one fully connected layer (“FC layer”). In medical imaging, it is critical that radiologists can trust that the visual explanations reflect the locations the model used to make predictions. Thus, HiResCAM has the potential to be useful and address previously unrecognized risks with the way that medical imaging machine learning models are often constructed and analyzed. The top half of the table includes studies that already incorporated visual explanation methods. The bottom half of the table includes studies that did not report results of a visual explanation method, but which use CNN models for a medical imaging classification task and thus could have a visual explanation method applied.

ple instance learning setup with a per-slice fully connected layer that produces per-slice predictions which are then averaged to yield the whole-volume predictions. In other words, BodyCAM follows the CAM architecture while AxialNet falls into the more general class of CNNs that end in one fully connected layer. Because BodyCAM follows the CAM architecture, CAM, Grad-CAM, and HiResCAM all produce identical explanations for BodyCAM. This is confirmed experimentally in Table 1 of the main paper, where HiResCAM and Grad-CAM yield the same OrganIOU.

We are encouraged by the result that AxialNet outperforms BodyCAM. While we recognize that the global av-

erage pooling step provides the convenient property of enabling input images of variable spatial dimensions, we also believe performance is important and that if eliminating global average pooling can provide better performance in some tasks then it is a direction worth exploring further. In future work, it would be interesting to systematically investigate the effect of removing the global average pooling step across a variety of architectures and imaging applications.

9. Literature review: how HiResCAM could benefit medical imaging explainability

This section includes examples of various studies that apply deep learning to medical imaging tasks to illustrate more clearly how our findings related to HiResCAM and CNNs ending in only one fully connected layer could positive impact explainability. Table 3 includes examples of previously published studies that apply machine learning to a medical imaging task. The table considers what architecture was used as well as any visual explanation method that was applied, and analyzes whether there was a risk of a visual explanation method providing the false impression that the model had highlighted the wrong location.

It appears that presently, there is real risk in medical imaging of relying on faulty visual explanations that highlight locations the model did not actually use, due to the popularity of Grad-CAM as a visual explanation method and the popularity of custom CNN architectures that end in more than one fully connected layer. In these studies, there are no experiments justifying the need for more than one fully connected layer. Most likely, the decision to include more than one fully connected layer was due to two factors: (a) the authors of these works are likely taking inspiration from architectures like VGG or AlexNet which include multiple fully connected layers; and (b) to the best of our knowledge, no prior work before ours conveys the potential explainability benefits of using only one fully connected layer at the end of a CNN. In all studies with high risk of wrong explanations, we recommend reducing the number of fully connected layers to one and using HiResCAM as the explanation approach to ensure that the visual explanations actually reflect the regions the model is using to make predictions.³

10. HiResCAM v.s. “other CAMs”: how gradient-based explanations differ from weakly-supervised segmentation

Many methods for weakly-supervised segmentation are based on CAM or Grad-CAM, including methods with “CAM” in the name like Mixup-CAM [11], Sub-Category CAM [12], and Puzzle-CAM [36], as well as other methods like Guided Attention Inference Network [44] and FickleNet [43].

However, there is a key philosophical difference between work in weakly-supervised segmentation and work in gradient-based explanation. The goal of weakly-supervised

³If keeping the number of layers the same is a priority, then a reduction in the number of fully connected layers could be accompanied by the addition of an equivalent number of convolutional layers before the final fully connected layer. If it is important not to further shrink the spatial dimensions of the representation, 1×1 convolutions could be used in these additional layers.

segmentation is to obtain a pixel-level segmentation mask using a classification model trained on only image-level labels. Because classifiers tend to focus on small discriminative parts of objects, a key goal of weakly-supervised segmentation methods is to expand the attention map of the classifier beyond the small discriminative areas so that the map covers more of the object. In contrast, the goal of work in gradient-based explanation is merely to explain what the model has done - even if that means highlighting areas outside of the object (*e.g.* if a model has used tracks to identify a train, or water to identify a boat), and even if that means highlighting only a small discriminative part of the object. HiResCAM is a gradient-based explanation method, with the main goal of providing explanations that faithfully represent the locations the model has used to make a prediction. Thus, the goal of HiResCAM is not to expand the attention maps, merely to provide reliable insight into the model’s behavior.

11. The bias term of the final fully connected layer has no effect on CAM visualizations

The authors of the original CAM paper state, “we ignore the bias term: we explicitly set the input bias of the softmax to 0 as it has little to no impact on the classification performance” [79]. In our experiments when calculating attention maps to obtain OrganIoU for BodyCAM, the bias term was not explicitly ignored, but we show here that there is no need to explicitly ignore the bias term because it drops out of the visualization on its own, thus supporting the CAM authors’ original observation that the bias term has no effect on the attention maps.

Section 6 demonstrated that HiResCAM is a generalization of CAM. Calculating the CAM map from the HiResCAM perspective illustrates why the bias term is irrelevant to the explanation in a CAM architecture. Consider the score s_m written in terms of the feature maps, for a final fully connected layer that does have a nonzero bias term:

$$s_m = w_m^1 \left(\frac{1}{D_1 D_2} \sum_{d_1=1}^{D_1} \sum_{d_2=1}^{D_2} \mathbf{A}_{d_1 d_2}^1 \right) \quad (23)$$

$$+ w_m^2 \left(\frac{1}{D_1 D_2} \sum_{d_1=1}^{D_1} \sum_{d_2=1}^{D_2} \mathbf{A}_{d_1 d_2}^2 \right) \quad (24)$$

$$+ \dots + w_m^F \left(\frac{1}{D_1 D_2} \sum_{d_1=1}^{D_1} \sum_{d_2=1}^{D_2} \mathbf{A}_{d_1 d_2}^F \right) + b. \quad (25)$$

When calculating the gradient $\frac{\partial s_m}{\partial \mathbf{A}^f}$, the bias term disappears, because it has nothing to do with \mathbf{A}^f . Thus, the formula for CAM (or HiResCAM) remains the same as it was in the previous section.

There is some intuition about why the bias term of the final fully connected layer should not affect the visualizations: the point of CAM is to show an explanation for a particular label and a particular input image. However, the bias term will be the same for every image in an arbitrary collection of images, because the bias term is part of the model and is not input-dependent. Therefore, the bias term must not contribute anything input-specific to the explanation for any particular input image.

12. Further motivation for the mask loss

The classification loss \mathcal{L}_{class} determines the extent of attention (*e.g.* a whole lung or only a lobe) in allowed regions, while the mask loss \mathcal{L}_{mask} discourages attention in forbidden regions.

Classification loss. The amount of attention placed within allowed regions, determined by \mathcal{L}_{class} , can vary from abnormality to abnormality. The model could attend to the entire allowed region (useful for diffuse abnormalities) or a small sub-part of the allowed region (useful for focal abnormalities).

Mask loss. The mask loss is

$$\mathcal{L}_{mask} = - \sum_{i: \mathcal{G}_{true}=0} \log(1 - \tilde{a}_i). \quad (26)$$

where \tilde{a}_i accesses all elements of $\tilde{\mathcal{A}} \in \mathbb{R}^{M \times H \times D_1 \times D_2}$, the model’s predicted attention, and $\mathcal{G}_{true} \in \{0, 1\}^{M \times H \times D_1 \times D_2}$ defines an allowed region for the attention for each abnormality.

The mask loss is half of a segmentation cross entropy objective [34], specifically the part of the objective where the ground truth is equal to 0. To minimize the mask loss the model must not increase the abnormality score using forbidden regions (where $\mathcal{G}_{true} = 0$), which are regions outside the organ(s) in which that abnormality is found in a particular scan. The portion of the full segmentation objective relating to $\mathcal{G}_{true} = 1$ is excluded because we do not want to force the model to attend to the entire relevant organ. This is because most abnormalities do not occupy the entire organ, especially focal abnormalities such as nodules and masses.

In practice we find that training with \mathcal{L}_{mask} is stable. We explored an alternative mask loss formulation based on an L_2 norm but found that its performance was inferior.

In future work it would be interesting to explore the use of a mask loss in natural images for which only an image-level ground truth is available and particular classes tend to appear in consistent locations - for example, road scenes, in which the sky tends to appear in the top half of the image while the road tends to appear in the bottom half.

Example: lung nodule in the right upper lobe. For a lung nodule in the right upper lobe, the mask loss will discourage the model from predicting this nodule using forbidden regions, *i.e.* anatomy anywhere outside of the right

lung. For example the mask loss will discourage the model from exploiting liver nodules to predict the lung nodule (in a patient with metastatic cancer, there may be cancerous nodules and masses in multiple organs, but to predict specifically “lung nodule” only the lungs should be used). If lobe segmentations were available, then the mask loss could be used to discourage the model from predicting the right upper lobe nodule using anatomy anywhere outside of the right upper lobe specifically, but there are no lung lobe segmentation masks available in the RAD-ChestCT data set and so we use our unsupervised whole organ segmentations instead. The goal of the classification loss is to enable the model to make a correct prediction, so the classification loss should encourage the model to predict the nodule from the sub-part of the right upper lobe in which it is actually found. Ideally, the final explanation from the model should cover the relevant part of the right upper lobe, and nowhere outside of the right lung.

Features in one organ providing clues for another organ. It is true that sometimes, features in one organ may provide clues for another organ, such as the case of the metastatic cancer patient described above. We split abnormalities that occur in multiple organs into different labels to encourage the model to learn differences between organs. Developing models to leverage relationships across organs while precisely distinguishing between them is an interesting direction for future work.

13. PARTITION: Creating an attention ground truth

The PARTITION approach to create \mathcal{G}_{true} , the allowed regions for each abnormality, combines location \times abnormality labels extracted from radiology reports with unsupervised organ segmentation, as shown in Figure 4 of the main paper. This section provides further details on PARTITION’s subcomponents.

13.1. Location \times abnormality labels

The first step in creating the attention ground truth \mathcal{G}_{true} is obtaining the location \times abnormality labels. The location \times abnormality labels are produced via a simple extension of SARLE, the publicly available rule-based automated label extraction method used to create the RAD-ChestCT abnormality labels [20]. SARLE was introduced and evaluated in prior work [20]. The first step of SARLE is phrase classification, in which each sentence of a free text report is analyzed using a rule-based system to distinguish between “normal phrases” (those that describe normality or lack of abnormalities) and “abnormal phrases” (those that describe presence of abnormalities). The second step of SARLE is a “term search” that searches for abnormality-related vocabulary within the “abnormal phrases” to identify which specific abnormalities are present. The handling

of negation in the first step of SARLE is highly effective, and when combined with the term search yields an average F-score of 0.976 [20]. SARLE is designed to be easily customizable through the addition of extra vocabulary to the term search. We leverage this customizability by adding location terms to the term search, to identify whether each abnormality is located in the lungs, heart, great vessels, mediastinum, or elsewhere. We also make use of the medical definitions of the abnormalities themselves. Many abnormalities reveal their locations by definition, *e.g.* “pneumonia” (lung inflammation) which can only occur in the lungs or “cardiomegaly” (enlarged heart) which can only occur in the heart. Specific examples of some of our extensions to SARLE’s term search are shown in Table 4.

Subdividing abnormalities by their location is necessary in order to know which organ segmentations(s) are relevant for that abnormality. Dividing by location also provides the benefit of defining a more medically relevant task. For example, calcification in the lungs is usually caused by calcified nodules or calcified granulomas [37], whereas calcification in the aorta is typically due to atherosclerosis [16]. A catheter in the lungs is often a pigtail catheter, *e.g.* to treat a pneumothorax [39], while a catheter in the superior vena cava (a great vessel) is a central venous catheter [29].

List of all abnormalities. Table 5 includes a full listing of all the abnormality labels used in this study.

13.2. Unsupervised segmentation

Motivation. The second step in creating the attention ground truth \mathcal{G}_{true} is obtaining the segmentations for the allowed regions. We propose an approach for unsupervised segmentation in chest CT volumes based on morphological image processing. We choose an unsupervised morphological image processing approach over a supervised machine learning approach for several reasons.

First, the unsupervised approach requires no manual annotations. In contrast, training a machine learning organ segmentation model on RAD-ChestCT would require manually circumscribing the relevant anatomical structures on hundreds or thousands of slices, a labor-intensive process that would take months of effort by a domain expert.

Second, the two largest organs we were interested in segmenting - the right lung and left lung - can be segmented with excellent performance using morphological image processing, because the lungs are large contiguous regions of mostly black pixels. In fact, morphological image processing yields such good results for lung segmentation that it was used to create the training set lung segmentation ground truth in the CT-ORG data set [55, 56, 14].

Finally, training a machine learning segmentation model on another dataset and then deploying it on RAD-ChestCT would be unlikely to result satisfactory performance on RAD-ChestCT due to significant differences in the data

distributions [19]. RAD-ChestCT consists of 36,316 non-contrast chest CT scans, 95% of which have a slice thickness <0.625 mm [20]. RAD-ChestCT includes a mixture of mild and severe lung diseases. The CT-ORG data set [55, 56, 14] includes 119 training and 21 test CT scans with labels for lung, bones, liver, kidneys, and bladder; the images come from contrast and non-contrast, low-dose and high-dose, abdominal and full body CT scans. The AAPM Thoracic Auto-segmentation Challenge 2017 data set [74, 75] includes 36 training cases and 24 test cases with labels for the esophagus, heart, lungs, and spinal cord; these scans are all contrast-enhanced with slice spacing of 1 mm, 2.5 mm, or 3 mm. Furthermore in AAPM 2017, cases with collapsed lungs from extensive disease were excluded, whereas these cases are included in RAD-ChestCT. Since we found the unsupervised segmentation approach effective for improving overall performance through the mask loss, we chose to use the results of the unsupervised segmentation and leave the challenging task of domain adaptation for machine-learning-based organ segmentation models for future work.

If the mask loss were to be used in training models on other body regions, such as the head, abdomen, or pelvis, it is likely that a machine learning organ segmentation model would be needed, as an unsupervised approach is less likely to perform well in these non-thorax body regions.

Proposed unsupervised segmentation approach. Our unsupervised multi-organ segmentation approach includes three stages. In the first stage both lungs are segmented together using morphological image processing, using the four steps shown in Figure 7. Next, a bounding box enclosing both lungs is computed and the right lung and left lung are separated via bisection along the midline sagittal plane. Finally, the mediastinum segmentation is defined as the center-left nonlung region inside of the lung bounding box, exploiting the anatomical relationship of the mediastinum and the lungs. The final output is a left lung segmentation, a right lung segmentation, and a mediastinum segmentation that includes the heart and great vessels. All segmentation code will be made publicly available.

Evaluation and quality control. We do not calculate intersection over union (IoU) of our organ segmentations on RAD-ChestCT because there are no ground truth organ segmentations available for RAD-ChestCT. We also do not calculate IoU of our RAD-ChestCT segmentation approach on the CT-ORG or AAPM data sets because of the significant differences in data distribution between RAD-ChestCT and CT-ORG or AAPM discussed earlier in this section. Like all morphological image processing approaches for lung segmentation, our unsupervised segmentation method is sensitive to threshold values that had to be optimized specifically for RAD-ChestCT. For example the minimum allowed volume size specified in step (4), removal of small objects, was

Input Sentence	Step 1 (Vanilla SARLE): Keep Only Abnormal Phrases	Step 2 (Vanilla SARLE): Identify Abnormality with Term Search	Step 3 (our addition): Identify Location with Term Search	Comment
the heart is enlarged without pericardial effusion	the heart is enlarged	cardiomegaly	heart	Step 2: "heart is enlarged" is one of the synonyms for the abnormality "cardiomegaly." Step 3: the word "heart" indicates heart as the location
there is a nodule in the right upper lobe	there is a nodule in the right upper lobe	nodule	right lung	Step 3: "right upper lobe" indicates "right lung" as the location
left pneumonia	left pneumonia	pneumonia	left lung	Step 3: "pneumonia" by definition only affects the lung, so "left pneumonia" implies the location "left lung"
calcifications in the aorta	calcifications in the aorta	calcification	great vessel	Step 3: the aorta is a great vessel
a calcified granuloma is visible in the apex of the left lung	a calcified granuloma is visible in the apex of the left lung	calcification, granuloma	left lung	
the catheter tip is visible in the SVC	the catheter tip is visible in the SVC	catheter or port	great vessel	Step 3: the superior vena cava (SVC) is a great vessel
The lungs are clear				normal finding; no abnormality labels produced
The consolidation has resolved				normal finding; no abnormality labels produced

Table 4. Examples of our addition to the previously published SARLE framework to identify the location of each abnormality from the radiology reports.

Corresponding Segmentation	Label
Right and/or Left Lung	air trapping, airspace disease, aspiration, atelectasis, bronchial wall thickening, bronchiectasis, bronchiolectasis, consolidation, emphysema, fibrosis (lung), groundglass, interstitial lung disease, lung infection, lung inflammation, lung scarring, lung scattered nodules or nodes, mucous plugging, plaque (lung), pleural effusion, pleural thickening, pneumonia, pneumothorax, pulmonary edema, reticulation, septal thickening, tree in bud, lung resection, lung transplant, postsurgical (lung), bandlike or linear, honeycombing, lung calcification, lung cancer, lung cavitation, lung cyst, lung density, lung granuloma, lung lesion, lung lucency, lung lymphadenopathy, lung mass, lung nodule, lung nodulegr1cm, lung opacity, lung scattered calcification, lung soft tissue, chest tube, lung catheter or port, lung clip, lung staple, lung suture
Mediastinum (includes Heart and Great Vessels)	cardiomegaly, heart failure, pericardial effusion, pericardial thickening, CABG, heart transplant, postsurgical (great vessel), postsurgical (heart), sternotomy, coronary artery disease, great vessel aneurysm, great vessel atherosclerosis, great vessel calcification, great vessel dilation or ectasia, great vessel scattered calc, heart atherosclerosis, heart calcification, heart scattered calc, mediastinum calcification, mediastinum cancer, mediastinum lymphadenopathy, mediastinum mass, mediastinum nodule, mediastinum opacity, great vessel catheter or port, heart catheter or port, heart stent, heart valve replacement, pacemaker or defib

Table 5. The 80 abnormality labels used in this study.

tuned to 1000000, a value that enables preservation of the right and left lung but elimination of the stomach in RAD-ChestCT. However, this threshold value is inappropriate for any data set that has a different resolution such that a single voxel corresponds to a different physical volume in the real world. Each threshold was chosen in an iterative process that involved manual inspection of hundreds of examples produced with different thresholds. Selecting new customized thresholds for CT-ORG or AAPM would thus not

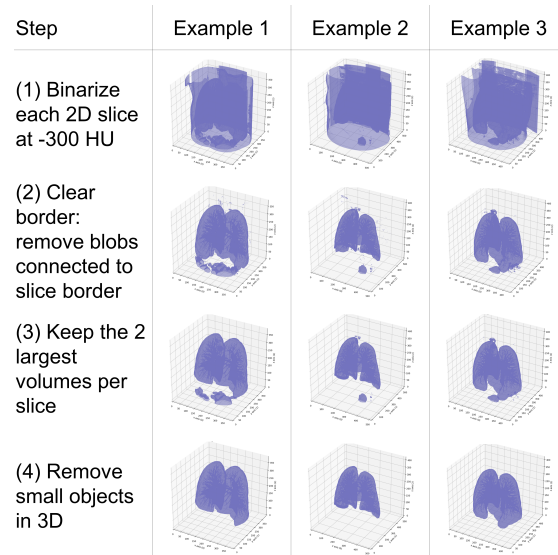


Figure 7. The unsupervised lung segmentation pipeline using morphological image processing illustrated with 3D volume renderings at each step, for 3 different CT volumes.

yield an evaluation that is reflective of our algorithm or its performance on RAD-ChestCT. A limitation of our work is that we did not manually create segmentation maps to calculate IoU for our unsupervised segmentation pipeline, due to the time consuming nature of creating segmentation ground truth in large 3D volumes. In future work, we would like to manually create this ground truth so that we can quantitatively evaluate our unsupervised segmentation with IoU. For now, we are encouraged by the performance benefit of using the unsupervised segmentation in the mask loss, as well as by the qualitative results for our segmentation approach, discussed next.

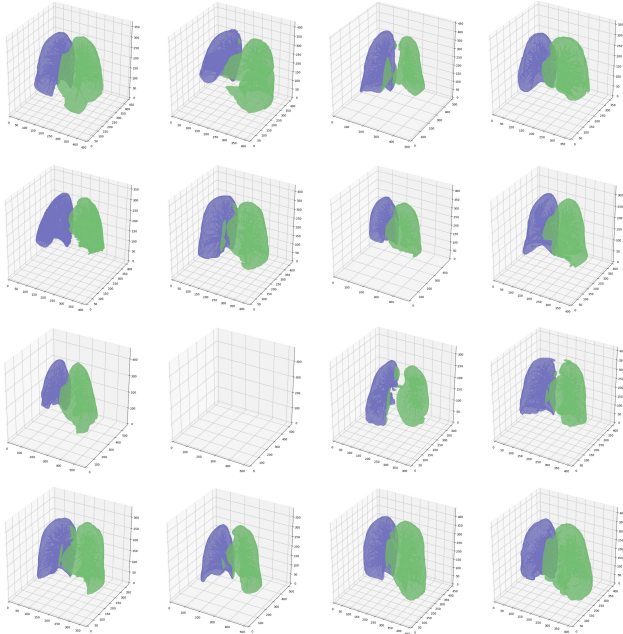


Figure 8. A random selection of right and left lung segmentations from our unsupervised segmentation method. The scan at row 3, column 2 where both lungs are missing is an example of a scan for which the unsupervised segmentation failed; for this scan a heuristic mask was used in computing the mask loss. Only 4% of scans require a heuristic mask.

Qualitative results. We undertook two steps to evaluate our unsupervised segmentation approach. First, we performed manual inspection of numerous randomly-selected segmentations, as 3D renderings and/or 2D projections along the axial, sagittal, and coronal planes. Several 3D renderings of randomly-selected right lung and left lung segmentations produced by our approach are shown in Figure 8. Next, we use summary statistics gathered from the training set to assess lung inclusion quality. Analysis of histograms of lung bounding box dimensions paired with visual inspection of outlier scans enabled definition of outlier thresholds that automatically identify when one or both lungs are missing due to severe disease. We quantified the fraction of segmentations in which one or both lungs is missing and found it to be only 4%, meaning that 96% of the segmentations pass this basic quality control metric. In creation of the attention ground truth, the 4% of segmentations that fail quality control are discarded and replaced with a heuristic mask in which the allowed region for the right lung is the right half of the volume, the allowed region for the mediastinum is the center half, and the allowed region for the left lung is the left half.

Attention ground truth and mask loss implementation details. In order to calculate the mask loss, the dimensions of the attention ground truth must match

AxialNet Performance with PARTITION Variants		
Downsampling Algorithm	Dilation	AUROC
Area	False	0.658
	True	0.662
Trilinear	False	0.661
	True	0.671
Nearest Neighbor	False	0.679
	True	0.654

Table 6. Validation set median AUROC for AxialNet $\mathcal{L}_{class} + \lambda\mathcal{L}_{mask}$ trained with different organ mask downsampling algorithms and dilation settings. A nearest neighbor downsampling algorithm without dilation achieved the best AUROC and so was used for all other AxialNet $\mathcal{L}_{class} + \lambda\mathcal{L}_{mask}$ experiments including those shown in the main paper. This experiment used the pre-defined RAD-ChestCT subset of 2,000 training volumes and 1,000 validation volumes [20].

the dimensions of the low-dimensional CT representation. Thus, the raw segmentation masks are downsampled to $\{0, 1\}^{H \times D_1 \times D_2}$. We compared nearest neighbors, trilinear, and area downsampling algorithms, with and without morphological dilation of the downsampled mask. The nearest neighbors algorithm with no dilation yielded the best performance (Table 6), so this setting was selected to create the attention ground truth used in the final mask loss implementation. For all models, the OrganIOU was calculated directly between the predicted attention $\hat{\mathcal{A}}$ and the attention ground truth \mathcal{G}_{true} . We explored calculation of OrganIOU in the input space using upsampling of the predicted attention but found this to be prohibitively computationally expensive (estimated >3 weeks of runtime per model).

To improve model training time, the attention ground truth was computed in default axial orientation during the first epoch and then loaded from disk for all subsequent epochs. The data augmentation transformations randomly applied to each CT scan in each epoch were applied dynamically to each sub-volume of that scan’s attention ground truth before the mask loss calculation.

14. PASCAL VOC 2012

Explanations overlap the related object more effectively in images with fewer labels. Figure 9 illustrates the HiResCAM IoU for the VGG-16 classifier across all epochs. The model achieves higher IoU on images that contain only one label, and lower IoU on images that contain multiple labels. This result suggests that for images containing multiple labels, the model could be exploiting correlations between labels in order to make predictions, which would lower the IoU by spreading the attention for each label beyond the borders of that label.

72 example explanations. Figure 11 provides

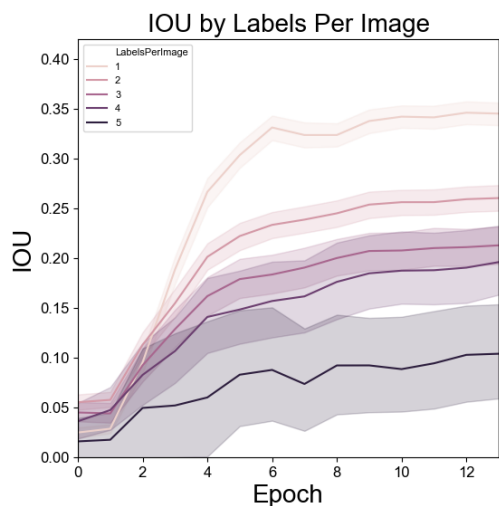


Figure 9. The PASCAL VOC 2012 validation set HiResCAM IoU throughout training for a VGG-16 classification model, split by the number of labels in the image. The IoU is consistently worse for images that contain multiple labels, and is best for images that contain only one label.

HiResCAM and Grad-CAM explanations for 72 randomly-selected validation set image-label pairs. While the location-focused HiResCAM explanations are more reflective of the locations the model is using, the feature-focused Grad-CAM explanations sometimes appear more expansive, a characteristic that could be exploited in future work for weakly-supervised segmentation. See Section 10 for a discussion of the difference between the goals of model explanation and weakly-supervised segmentation.

15. RAD-ChestCT

15.1. Abnormality scores across slices reflect medical concepts

As noted in the main text, the matrix of all per-slice abnormality scores $\mathbf{C} \in \mathbb{R}^{M \times H}$ from AxialNet contributes to model explainability by illustrating which axial slice groups contribute most to the prediction of each abnormality. We demonstrate in Figure 12 that \mathbf{C} displays patterns consistent with medical knowledge. Analysis of the figure is provided in the caption.

15.2. Examples of HiResCAM attention maps for incorrect predictions

As mentioned in the main paper, 79% of the time the attention maps for incorrect predictions make it obvious that the model was incorrect. Figure 10 provides examples of HiResCAM explanations for incorrect predictions of the AxialNet $\mathcal{L}_{class} + \lambda\mathcal{L}_{mask}$ model.

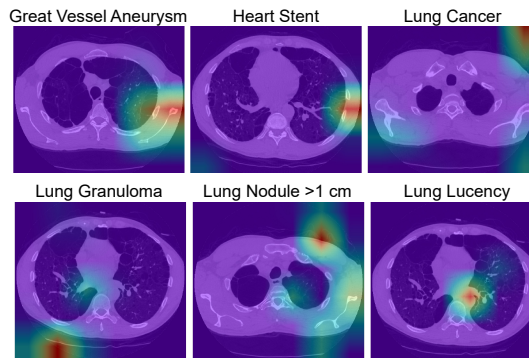


Figure 10. Examples of HiResCAM attention maps for incorrect predictions of the AxialNet $\mathcal{L}_{class} + \lambda\mathcal{L}_{mask}$ model, which make it apparent that the model was wrong by demonstrating that the model focused on the wrong anatomical structure or outside the body entirely.

15.3. Great vessel atherosclerosis case study

Figure 13 provides a case study for the abnormality label “great vessel atherosclerosis” that illustrates how visual explanations can demonstrate when a model is exploiting correlations to make a prediction. Additionally, the case study shows how the mask loss discourages exploitation of confounding variables. Analysis of the case study is provided in the figure caption.

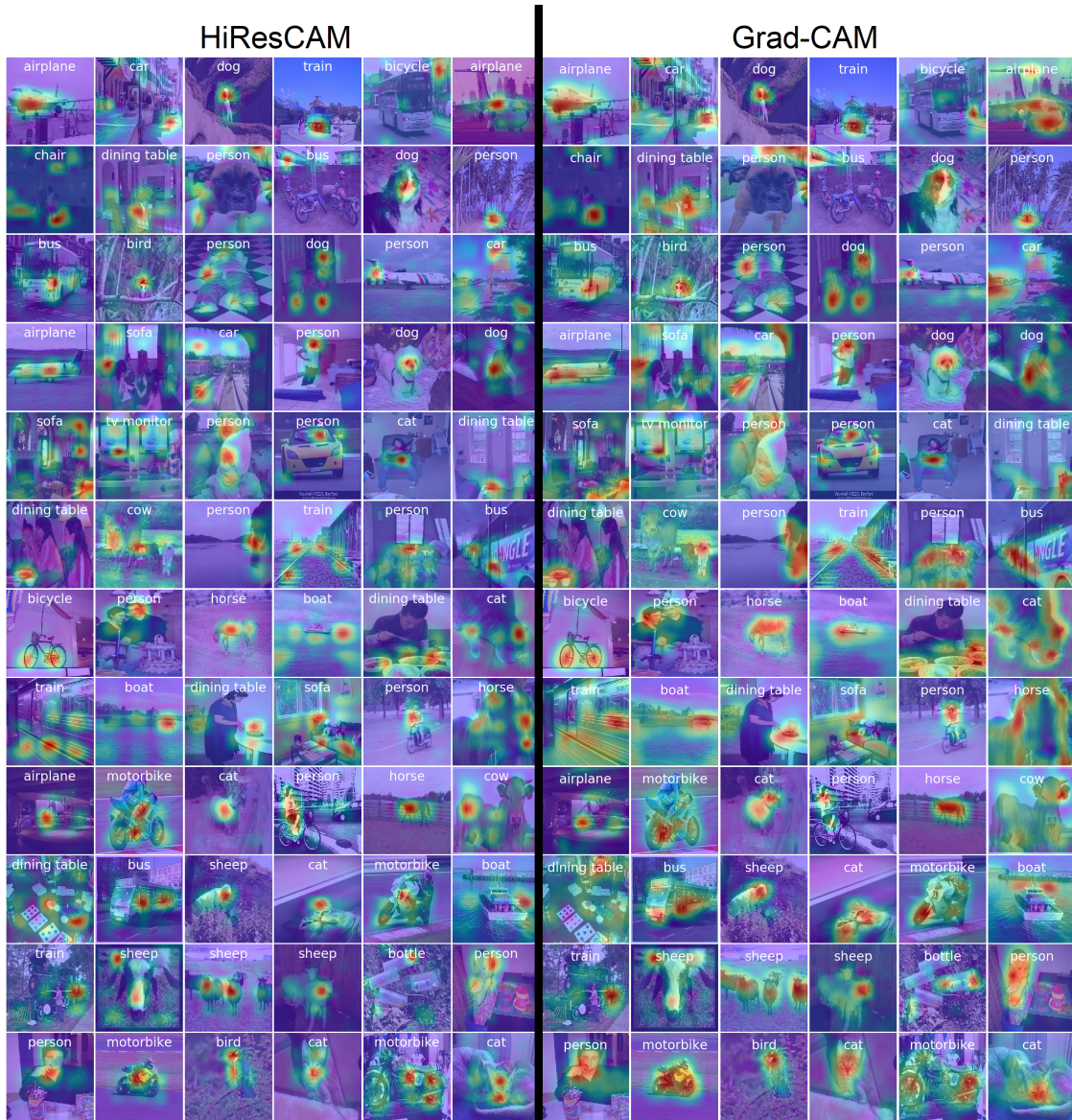


Figure 11. HiResCAM and Grad-CAM explanations for 72 randomly-selected PASCAL VOC 2012 validation set image-label pairs. The explanations are for a VGG-16 model with convolutional layers pretrained on ImageNet and all layers refined on PASCAL VOC 2012. Each half of the figure includes the same images and labels. The two halves differ only in the calculation of the explanation. VGG-16 was chosen because it is a commonly used network that has been used with Grad-CAM before. Grad-CAM’s tendency to expand the attention may be useful for weakly supervised segmentation. However, in medical imaging, understanding of where the model is looking is paramount, so HiResCAM paired with a CNN ending in one fully connected layer is a better choice than Grad-CAM (see Section 10).

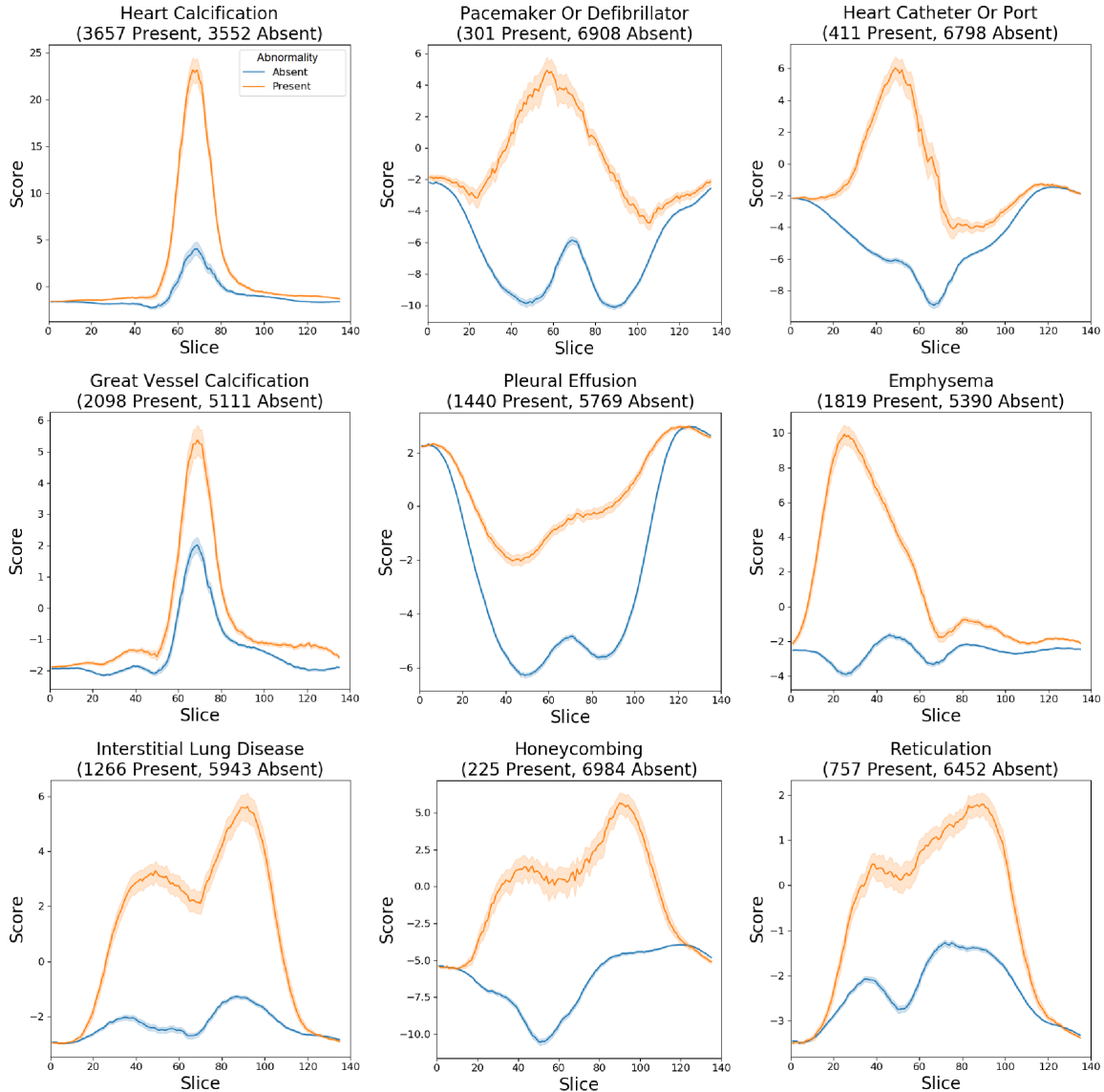


Figure 12. Summary of the per-slice abnormality scores $\mathbf{C} \in \mathbb{R}^{M \times H}$ across the 7,209 RAD-ChestCT test set CT volumes, for 9 example abnormalities. The matrices \mathbf{C} were calculated for each test set scan using the final AxialNet $\mathcal{L}_{class} + \lambda \mathcal{L}_{mask}$ whole dataset model. The orange line depicts the mean score and 95% confidence interval for scans in which the listed abnormality is present, while the blue line depicts the mean score and 95% confidence interval for the scans in which the abnormality is absent. Slice group 0 is closer to the head, while slice group 135 is closer to the abdomen. **Analysis:** Several interesting trends are apparent. **(General)** The orange line for scans containing the abnormality is higher than the blue line for scans lacking the abnormality, indicating higher scores when the abnormality is present, as desired. **(Top Row)** Example heart abnormalities shown on the top row tend to have peak scores in central slices where the heart is found. Furthermore, the scores for “heart calcification” and “great vessel calcification” have a similar distribution across slices, which is reasonable since these abnormalities are related - though great vessel calcification scores are comparatively higher in slices 80+, which makes sense as the aorta (a great vessel) descends into the abdomen. **(Pleural Effusion)** For “pleural effusion,” the model tends to yield high scores towards the lower section of the chest cavity (\approx slices 80-120), which is reasonable because pleural effusions frequently collect in the pleural spaces next to the lung bases. The high scores for pleural effusion in the upper lungs may be an artefact of symmetry - the model may have learned to find the lung bases through a relative decrease in the proportion of the slice occupied by lung tissue, and is detecting this relative decrease again at the apices. **(Emphysema)** The emphysema scores peak towards the upper lobes of the lungs (\approx slices 0-50), which is consistent with the fact that the commonest form of emphysema (centrilobular emphysema) is typically most visible in the upper lungs [66]. **(Bottom Row)** Interstitial lung disease, honeycombing, and reticulation, when present, have high predicted scores throughout the entire lung field, which is reasonable as all of these abnormalities are lung abnormalities that tend to be diffuse [64].

Great Vessel Atherosclerosis Case Study

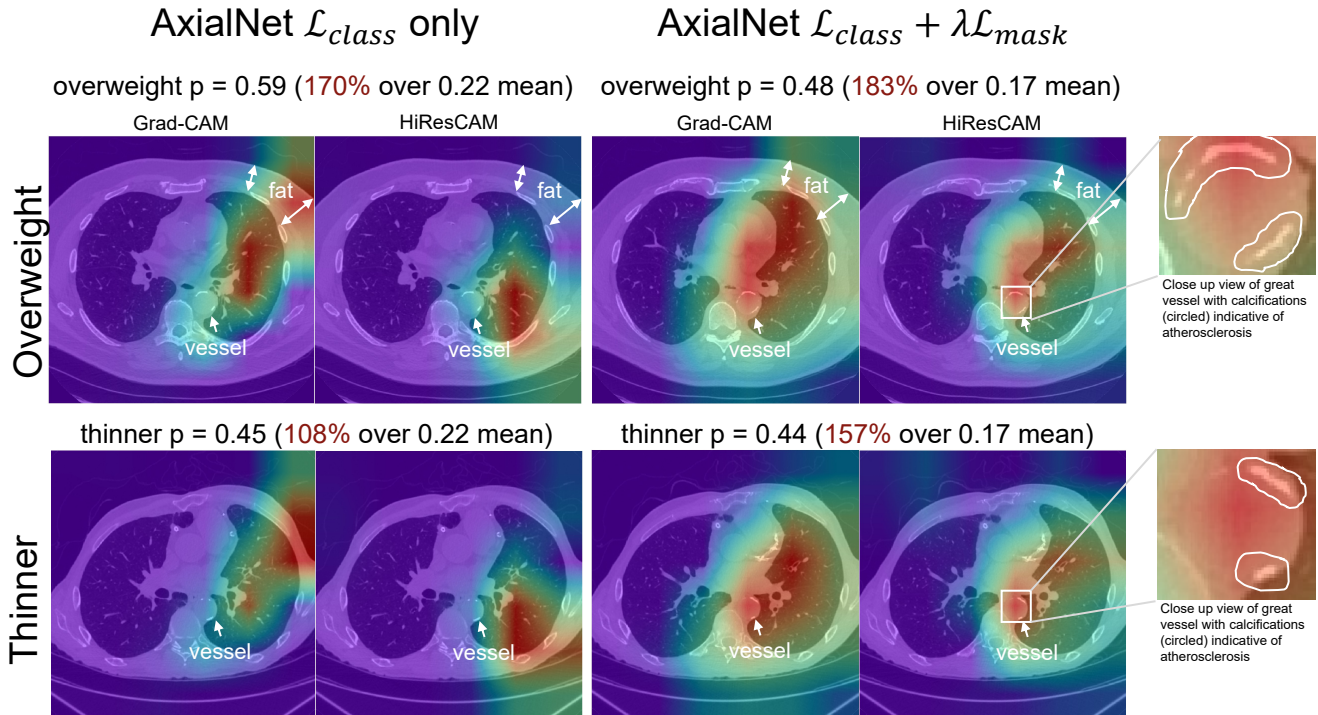


Figure 13. Great vessel atherosclerosis case study that illustrates how visual explanations can illuminate when a model is inappropriately exploiting correlations to make predictions, and additionally how the mask loss discourages exploiting confounding variables. Anatomy annotations added for clarity. Best viewed in color. **Analysis:** (Top Row) The top row depicts an overweight patient for which both the AxialNet \mathcal{L}_{class} and AxialNet $\mathcal{L}_{class} + \lambda\mathcal{L}_{mask}$ models predict high likelihood of atherosclerosis (probabilities 170% and 183% above the mean prediction for this label, respectively). Inspection of the attention maps suggest that AxialNet \mathcal{L}_{class} may be exploiting the fat content in the body wall to make the prediction, as the attention overlaps this fat layer. The AxialNet $\mathcal{L}_{class} + \lambda\mathcal{L}_{mask}$ model in contrast appears to be focusing more on the great vessel itself. High fat in the body wall (*i.e.*, overweight or obesity) is a known risk factor for atherosclerosis [76]. However, it is inappropriate to directly use a patient’s weight to predict atherosclerosis, because it is possible to be overweight without great vessel atherosclerosis and it is also possible to have great vessel atherosclerosis without being overweight. Great vessel atherosclerosis should be diagnosed by inspecting the great vessel itself for signs of atherosclerosis, which include calcifications like those circled on the right of the figure. (Bottom Row) The bottom row illustrates how the AxialNet \mathcal{L}_{class} model’s strategy of exploiting the patient’s obesity can backfire. The bottom row shows a thinner patient who still has great vessel atherosclerosis in spite of their lower body fat. Here, the AxialNet \mathcal{L}_{class} model again places too much focus on the body wall and produces a score only 108% above average in spite of the severe atherosclerosis visible in the vessel itself. In contrast, the AxialNet $\mathcal{L}_{class} + \lambda\mathcal{L}_{mask}$ model focuses more on the great vessel itself and produces a score 157% above average in spite of the patient’s thinner body habitus. The mask loss discouraged the model from exploiting the body wall for prediction, and was thus able to produce a model that appears to have used more actual signs of atherosclerosis in the vessel to make the prediction.